Fuel 224 (2018) 186–209

Contents lists available at ScienceDirect

Fuel

journal homepage: www.elsevier.com/locate/fuel

Flow topology distribution in head-on quenching of turbulent premixed flame: A Direct Numerical Simulation analysis

Jiawei Lai[a,*], Daniel H. Wacks[b], Nilanjan Chakraborty[a]

[a] School of Mechanical and Systems Engineering, Newcastle University, Claremont Road, Newcastle NE1 7RU, UK
[b] Department of Engineering, Durham University, Lower Mountjoy, Stockton Road, Durham DH1 3LE, UK

ARTICLE INFO

Keywords:
Flow topology
Turbulent premixed flames
Direct Numerical Simulation

ABSTRACT

The distribution of flow topologies within the flame, and their evolution with flame quenching have been analysed using a Direct Numerical Simulation (DNS) database of head-on quenching of statistically planar turbulent premixed flames by isothermal inert walls for different values of turbulence intensity and global Lewis number. It has been found that dilatation rate plays a key role in determining the flow topology distribution within the flame and this dilatation rate field is significantly affected by the flame quenching in the vicinity of the wall. The influence of the wall on the dilatation rate field in turn affects the statistical behaviour of all three invariants of the velocity gradient tensor and the distribution of flow topologies. The effects of heat release and thermal expansion strengthen with decreasing Lewis number which give rise to an increase in the probability of obtaining topologies which are specific to high positive values of dilatation rate. As the magnitude of positive dilatation rate and the likelihood of obtaining it decrease with flame quenching, the probability of finding the topologies, which are obtained only for positive values of dilatation rate, decreases close to the wall. The interrelation between the flow and flame topologies has been analysed in terms of Gaussian flame curvature and mean of principal flame curvatures. The contributions of individual flow topologies on the mean behaviour of wall heat flux magnitude, and the scalar-turbulence interaction and vortex-stretching terms in the scalar dissipation rate and enstrophy transport equations, respectively have been analysed in detail and dominant flow topologies which dictate the mean behaviours of these quantities have been identified. Detailed physical explanations have been provided for the observed flow topology distribution and its contribution to the scalar-turbulence and vortex-stretching terms. The nodal flow topologies have been found to be the significant contributors to the wall heat flux magnitude during head-on quenching of turbulent premixed flames irrespective of the value of global Lewis number.

1. Introduction

Flow topologies are often characterised in terms of a three-dimensional space made up of the three invariants (i.e. first P, second Q and third R) of the velocity gradient tensor $\partial u_i/\partial x_j$ [1,2], where u_i is the ith component of the velocity vector. The topologies are schematically shown in Fig. 1. To date, most analyses on flow topologies have been carried out for non-reacting incompressible flows. For incompressible flows the first invariant P is identically zero so the flow topology distribution is governed by Q and R. The analyses by Perry and Chong [1] and Soria et al. [3] indicated the topology $S4$ is predominantly obtained for positive values of second-invariant Q. Blackburn et al. [4] revealed that the topologies $S2$ and $S4$ remain dominant away from the wall for incompressible flows. It has been demonstrated by Chong et al. [5] and Chacin and Cantwell [6] that the joint probability density function (pdf) shows a "teardrop" structure, and subsequently Ooi et al. [7] provided the evidence regarding the universality of this "teardrop" structure in Q−R space. The physical explanations behind this "teardrop" structure of the Q−R joint pdf for incompressible flows have been provided by Elsinga and Marusic [8]. Both numerical and experimental investigations suggested that the "teardrop" structure of the Q−R joint pdf exists only in the fully turbulent region and not in the interface between turbulent and non-turbulent regions [5,6]. The qualitative arguments for predominant physical mechanisms associated with individual topologies (e.g. enstrophy production is large in $S4$ topology whereas the strain rate production is associated with $S1$ topology) were postulated by Tsinober [9]. The interaction of flow topologies with passive scalar surface topology can be quantified in terms of Gauss and mean curvatures (i.e. κ_g and κ_m) and was analysed in detail by Dopazo et al. [10]. It is worth noting that all the aforementioned analyses were

* Corresponding author.
E-mail address: j.lai@newcastle.ac.uk (J. Lai).

https://doi.org/10.1016/j.fuel.2018.03.021
Received 27 February 2017; Received in revised form 1 March 2018; Accepted 5 March 2018

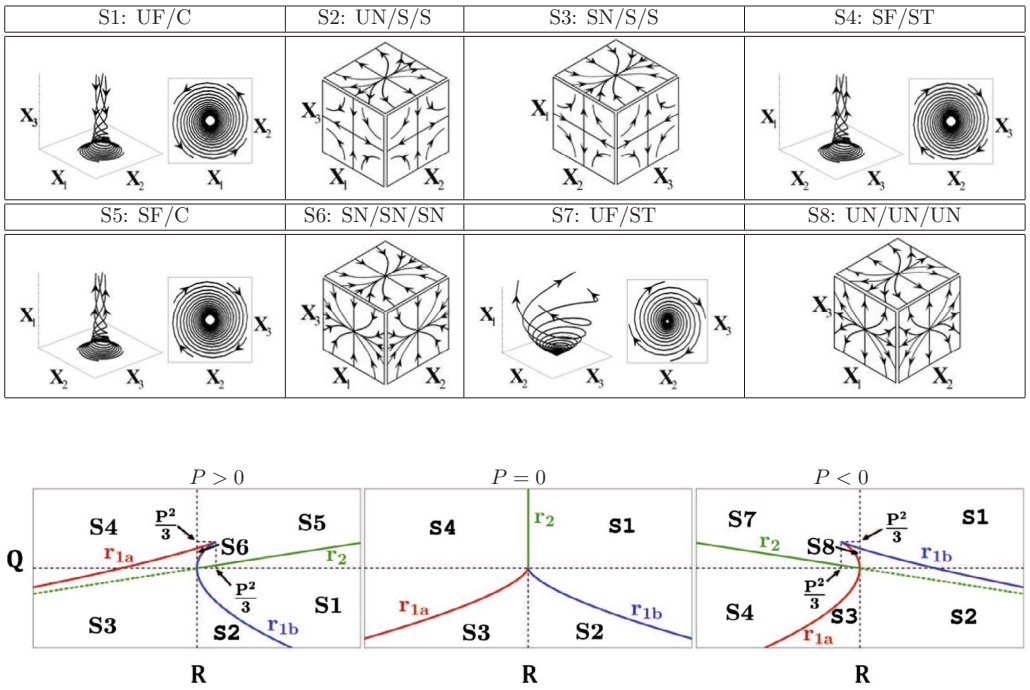

Fig. 1. Classification of $S1-S8$ topologies (UF = unstable focus, UN = unstable node, SF = stable focus, SN = stable node, S = saddle, C = compressing, ST = stretching) in the $Q-R$ plane with the lines r_{1a},r_{1b} and r_2 dividing the topologies, and black daksed lines indicates $Q = R = 0$.

conducted for incompressible fluids where the first invariant P is identically zero. However, in compressible flows the statistical behaviour of the first invariant of the velocity gradient tensor P plays an important role, and thus the co-ordinates in three-dimensional $P-Q-R$ space determine the local flow topology. The structure of a compressible wake, using the critical point theory in terms of P,Q and R, was analysed by Chen et al. [11] for the very first time. Sondergaard et al. [12] characterised small-scale local flow topologies in a compressible turbulent shear flow in terms of P,Q and R. Maekawa et al. [13] and Suman and Girimaji [14] demonstrated that $S2$ and $S4$ topologies are predominant on $Q-R$ plane for decaying isotropic compressible turbulence. The topology distributions in the inner and outer layers in turbulent compressible boundary layers were analysed using Direct Numerical Simulation (DNS) data by Wang and Lu [15]. It is worth noting that all these analyses were carried out for non-reacting flows.

Tanahashi et al. [16] was the first to analyse the flow topologies in turbulent premixed flames in order to distinguish between strain dominated and vorticity dominated regions. Grout et al. [17] analysed flow topologies using decaying turbulence DNS data of a reacting transverse fuel jet in cross-flow, and revealed that $S8$ topology is associated with the regions of high heat release. Recently, Cifuentes and his co-workers [18,19] analysed the distribution of flow topologies across the flame front using simple chemistry DNS database of premixed turbulent flames with unity Lewis number representing the flamelets regime of combustion under decaying turbulence and reported that the probabilities of finding focal (nodal) flow topologies decrease (increase) across the flame front. Flow topology distributions in turbulent spray flames were analysed by Wacks and Chakraborty [20] using DNS data, which demonstrated that the flow topology distribution within the spray flames shows some resemblance to the findings by Cifuentes et al. [18] and Grout et al. [17]. Recently, Wacks et al. [21] analysed flow topology distributions for the different regimes of turbulent premixed combustion and it has been found that the weakening of dilatation rate (in other words weakening of P) from the corrugated flamelets to the thin reaction zones to the broken reaction zones regimes of premixed turbulent combustion plays a key role in the behaviours of the invariants of the velocity gradient tensor and their components, which in turn affects the distribution of flow topologies and their contributions to the evolutions of enstrophy and scalar dissipation rate. In this respect, it is useful to note that all the flow topology analyses for turbulent reacting flows were carried out for both steady and unsteady flow conditions which are not wall-bounded. The presence of a cold wall is essential for the structural integrity of the combustor, but the heat loss through the wall gives rise to flame quenching. Thus, the presence of a wall is expected to affect the dilatation rate and thus the behaviour of the first invariant of the velocity gradient tensor P. Poinsot et al. [22] indicated that the presence of wall significantly affects the vorticity and enstrophy distributions close to the wall during head-on quenching of turbulent premixed flames. The aforementioned discussion suggests that the flow topology in the region close to the wall is likely to be affected by the presence of the flame and its quenching. To date, considerable effort has been made to analyse flame-wall interaction based on numerical investigations [22–35], but none of these analyses focussed on the flow topology distribution in the near-wall region during unsteady wall-induced flame quenching. This gap in the existing literature is addressed here by analysing the statistical behaviours of the invariants of the velocity gradient tensor $\partial u_i/\partial x_j$ and flow topology distributions at different instants of time as the flame approaches the isothermal wall in the case of head-on quenching of statistically planar turbulent flames with different values of global Lewis number Le (i.e. $Le = 0.8-1.2$). For this purpose an existing DNS database [30–35] of head-on quenching of statistically planar turbulent premixed flames for different values of turbulence intensity and global Lewis number has been considered. All the flow topologies shown in Fig. 1 are associated with particular combinations of strain rate and vorticity distributions, and they can influence the local alignment of the principal strain rate and scalar gradient and vorticity, which in turn affect the statistical behaviours of the scalar-turbulence interaction and vortex-stretching terms. Moreover, vortex-stretching mechanism is of pivotal importance to the energy cascade in turbulent flows [36] and it plays a leading order role in the enstrophy transport in turbulent premixed combustion even though some other physical mechanisms (e.g. baroclinic torque) might also play leading roles alongside the vortrex-stretching term [35]. For the above reasons, the contributions of flow topologies on the scalar-turbulence interaction and vortex-stretching terms in addition to the wall heat flux magnitude at different stages of

head-on quenching have been analysed in this analysis. The contributions of flow topologies on flame-turbulence interaction and vortex-stretching terms, and wall heat flux magnitude provide information on the underlying key dominant canonical flow structures. This, in turn, helps to design simple experimental configurations representing dominant flow topologies to gain further physical insights and model validation. Moreover, it will enable numerical modellers to conduct Reynolds Averaged Navier-Stokes (RANS) and Large Eddy Simulations (LES) for simple representative flow configurations, which should be convenient for the model development. The main objectives of this analysis are:

- To demonstrate the influence of the wall on flow topology distribution and statistical behaviours of P,Q and R during head-on quenching.
- To provide the physical explanations for the observed behaviours of P,Q and R, and the flow topology distribution.
- To indicate the implications on these behaviours of vortex-stretching, flame normal straining and wall heat flux during head-on quenching of turbulent premixed flames.

The mathematical background related to the flow topology is presented in the next section, which is followed by a brief discussion of numerical techniques used to generate the DNS data. Following this, results will be presented and discussed. The conclusions will be drawn and main findings will be summarised in the final section of this paper.

2. Mathematical background

The local flow topologies are characterised by the invariants of the velocity-gradient tensor [1,2]:

$$A_{ij} = \frac{\partial u_i}{\partial u_j} = S_{ij} + W_{ij} \tag{1}$$

where the symmetric strain-rate tensor is $S_{ij} = 0.5(A_{ij} + A_{ji})$ and the anti-symmetric rotation rate tensor is $W_{ij} = 0.5(A_{ij} - A_{ji})$. The eigenvalues of A_{ij} are λ_1,λ_2 and λ_3 which are the solutions of the characteristics equation $\lambda^3 + P\lambda^2 + Q\lambda + R = 0$ with its invariants P,Q and R as specified below [1,2]:

$$P = -tr(A_{ij}) = -(\lambda_1 + \lambda_2 + \lambda_3) = -S_{ii} \tag{2}$$

$$Q = \frac{1}{2}([\mathrm{tr}(A_{ij})]^2 - \mathrm{tr}(A_{ij}^2)) = \frac{1}{2}(P^2 - S_{ij}S_{ij} + W_{ij}W_{ij}) = Q_S + \underbrace{W_{ij}W_{ij}/2}_{Q_W} \tag{3}$$

$$R = -\det(A_{ij}) = \frac{1}{3}(-P^3 + 3PQ - S_{ij}S_{jk}S_{ki} - 3W_{ij}W_{jk}S_{ki}) \tag{4}$$

The terms $Q_S = 0.5(P^2 - S_{ij}S_{ij})$ and $Q_W = 0.5(W_{ij}W_{ij})$ are the second invariants of the strain rate (i.e. symmetric part of $\partial u_i/\partial x_j$) and rotation rate (i.e. anti-symmetric part of $\partial u_i/\partial x_j$) tensors. The discriminant D, shown in the equation below, divides the $P-Q-R$ phase space into two regions: A_{ij} shows a focal topology for $D > 0$ region and it displays a nodal topology for $D < 0$ region [1,2]:

$$D = \frac{1}{108}[27R^2 + (4P^3 - 18PQ)R + 4Q^3 - P^2Q^2] \tag{5}$$

The surface $D = 0$ leads to two surfaces r_{1a} and r_{1b} in the $P-Q-R$ phase space:

$$r_{1a} = \frac{1}{3}P\left(Q - \frac{2}{9}P^2\right) - \frac{2}{27}(-3Q + P^2)^{3/2} \tag{6}$$

$$r_{1b} = \frac{1}{3}P\left(Q - \frac{2}{9}P^2\right) + \frac{2}{27}(-3Q + P^2)^{3/2} \tag{7}$$

Additionally, A_{ij} has purely imaginary eigenvalues on the surface r_2 which is given by $R = PQ$. The surfaces r_{1a},r_{1b} and r_2 divide the $P-Q-R$ phase space into the 8 distinct flow topologies as shown in Fig. 1.

3. Numerical implementation

A well-known DNS code SENGA [37] has been used for solving standard non-dimensional conservation equations of mass, momentum, energy and species for compressible reacting flows. A single step Arrhenius type irreversible chemistry is taken to represent the chemical mechanism for the purpose of computational economy because detailed chemistry three-dimensional simulations remain still extremely expensive [38] for a detailed parametric analysis as carried out in this paper. The simulation domain has been taken to be a rectangular box of $70.6\delta_Z \times 35.2\delta_Z \times 35.2\delta_Z$ which is discretised using a Cartesian grid of $512 \times 256 \times 256$ with uniform grid spacing in each direction. Here $\delta_Z = \alpha_{T0}/S_L$ is the Zel'dovich flame thickness with α_{T0} and S_L being the thermal diffusivity of the unburned gas and the unstrained laminar burning velocity respectively. The grid spacing used here ensures about 10 grid points across the thermal flame thickness $\delta_{th} = (T_{ad} - T_0)/\mathrm{Max}|\nabla\widehat{T}|_L$, where $\widehat{T}$,T_0 and T_{ad} are the dimensional instantaneous, unburned gas and adiabatic flame temperatures respectively. A non-slip isothermal inert wall with temperature $T_W = T_0$ is placed at $x_1 = 0$, where zero mass flux is enforced in the wall normal direction. The boundary opposite to the isothermal wall is considered to be partially non-reflecting, which is specified using the Navier Stokes Characteristic Boundary Conditions (NSCBC) technique [39]. The mean direction of flame propagation is aligned with the x_1-direction and the boundaries in the transverse directions (i.e. x_2 and x_3 directions) are taken to be periodic. The spatial differentiation for internal grid points has been conducted using a 10th order central difference scheme, and the order of differentiation gradually decreases to a one-sided 2nd order scheme at the non-periodic boundaries [37]. A third-order low storage Runge-Kutta scheme is used for explicit time advancement [40].

For the purpose of initialisation of reacting flow field, a steady unstrained planar laminar premixed flame solution has been used so that the $T = (\widehat{T} - T_0)/(T_{ad} - T_0) = 0.9$ isosurafce remains at a distance $20\delta_Z$ away from the wall. A homogeneous isotropic field of turbulent velocity fluctuations generated using a pseudo-spectral method [41] following the Batchelor-Townsend Spectrum [42] is used for initialization of the turbulent velocity field. However, the velocity components at the wall u_1, u_2 and u_3 are specified to be zero to ensure the no-slip condition. The initial velocity field is allowed to evolve for an initial eddy turn-over time before interacting with the flame.

The initial values of normalised root-mean-square (rms) turbulent velocity fluctuation u'/S_L, the ratio of turbulent integral length scale to thermal flame thickness l/δ_{th} for the turbulent velocity field away from the wall are summarised in Table 1 along with the corresponding values of Damköhler number (i.e. $Da = lS_L/\delta_{th}u'$) and Karlovitz number (i.e. $Ka = (u'/S_L)^{3/2}(l/\delta_{th})^{-1/2}$). It can be seen from Table 1 that the cases A, C and E (B, C and D) have same values of Da (Ka). All the cases nominally represent the thin reaction zones regime combustion according to the regime diagram by Peters [43]. Three different global Lewis numbers (i.e. Le = 0.8,1.0 and 1.2) have been considered for each set of turbulence parameters listed in Table 1. Standard values are considered for Prandtl number Pr and ratio of specific heats γ (i.e. $Pr = 0.7$ and $\gamma = 1.4$). The heat release parameter $\tau = (T_{ad} - T_0)/T_0$, and Zel dovich number $\beta = T_{ac}(T_{ad} - T_0)/T_{ad}^2$ are taken to be 6.0 (i.e. $\tau = 6.0$ and $\beta = 6.0$) where T_{ac} is the activation temperature. In the present analysis, the chemical mechanism and thermo-physical transport have been

Table 1
List of initial simulation parameters and non-dimensional numbers.

Case	A	B	C	D	E
u'/S_L	5.0	6.25	7.5	9.0	11.25
l/δ_{th}	1.67	1.44	2.5	4.31	3.75
Da	0.33	0.23	0.33	0.48	0.33
Ka	8.67	13.0	13.0	13.0	19.5

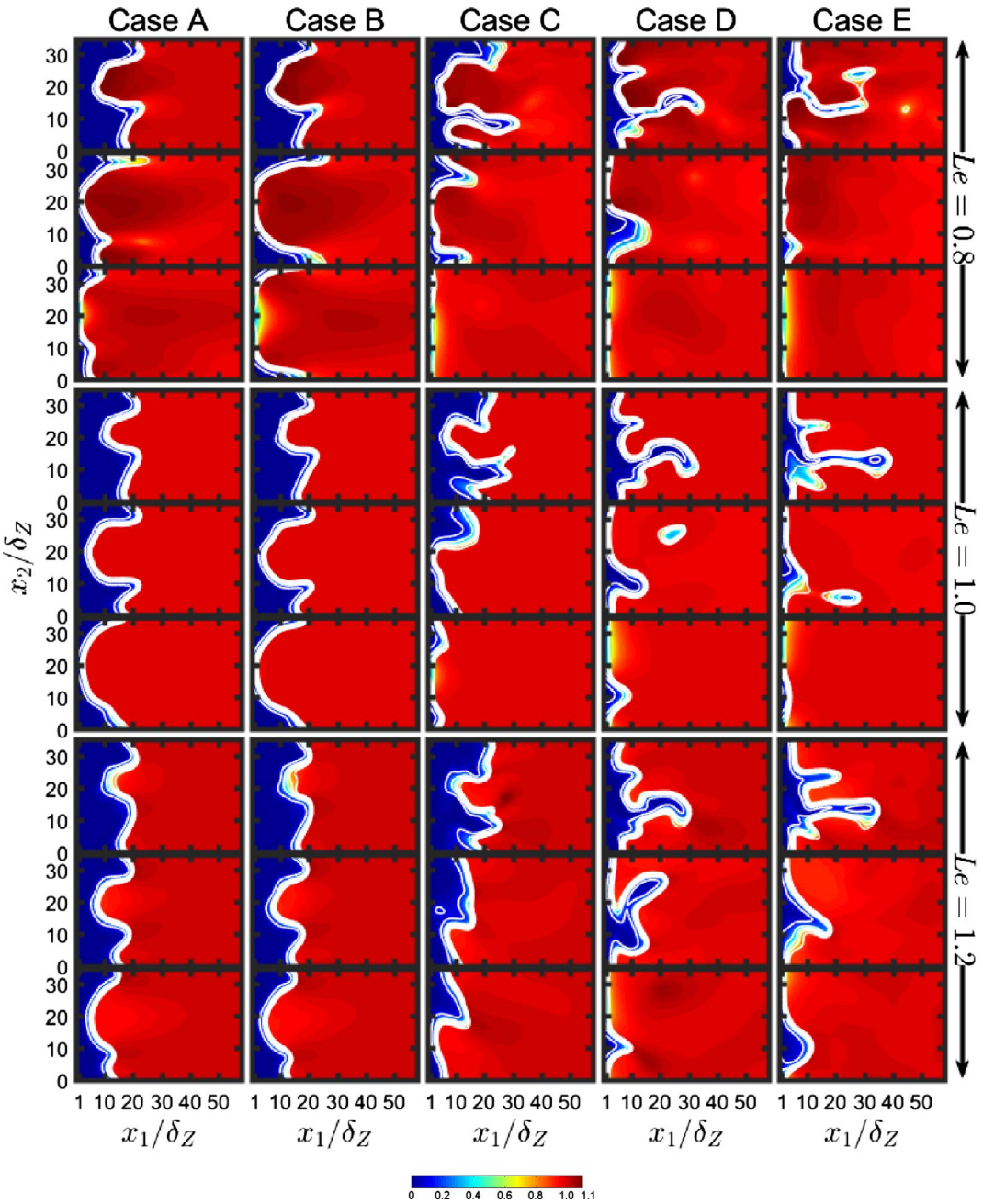

Fig. 2. Instantaneous non-dimensional temperature T fields for cases A–E (1st–5th column) at $t = 2\delta_Z/S_L$, $4\delta_Z/S_L$ and $6\delta_Z/S_L$ (1st–3rd row), white line presents c field from 0.1 to 0.9 with internal of 0.2 from left to right.

simplified for the purpose of computational economy. This was especially needed because of the simultaneous requirements of resolving the flame thickness and near-wall turbulence structures. These simplifications are not expected to affect the analysis reported in this paper in a significant manner because the current study focuses principally on the fluid-dynamical aspects of turbulent reacting flows, and this was demonstrated by several previous analyses [44–46]. In an actual combustion process, the temperature dependence of thermo-physical properties may lead to the variations of Prandtl and Lewis numbers of the major species within the flame. However, several previous analytical [47–49] and DNS [50–62] considered a single characteristic Lewis number and made assumptions similar to the ones used in this study for the purpose of simplicity and also for the analysis of Lewis number effects in isolation. Moreover, experimental studies [63–65] successfully used the concept of a characteristic Lewis number, where the global characteristic value of Lewis number was defined in terms of the Lewis number of the deficient species [63], or by heat release measurements [64], or by a linear combination of the mole fractions of the mixture constituents [65]. The simulations for turbulent cases have been carried out up to a time when the maximum, mean and minimum values of wall heat flux assume identical values following the flame quenching. The simulation time remains different from one case to another, but the simulations for all cases were continued for $t \geq 12\delta_Z/S_L$ where $12\delta_Z/S_L$ corresponds to 21, 30, 21, 15 and 21 initial eddy turn over times for cases A–E respectively. The non-dimensional grid spacing next to the wall $y^+ = u_\tau \Delta x/\nu$ remains smaller than unity for all turbulent cases (the maximum value of y^+ has been found to be 0.93 during the course of the simulation), where $u_\tau = \sqrt{\tau_w/\rho}$, τ_w and ν are the friction velocity, mean wall shear stress, and kinematic viscosity respectively. For $y^+ = u_\tau \Delta x/\nu \approx 0.93$, the minimum normalised wall

Table 2
List of normalised flame surface area A_T/A_L and turbulent flame speed S_T/S_L at different stages of flame quenching for all cases considered here.

		A		B		C		D		E	
	$\frac{tS_L}{\delta_Z}$	$\frac{A_T}{A_L}$	$\frac{S_T}{S_L}$	$\frac{A_T}{A_L}$	$\frac{S_T}{S_L}$	$\frac{A_T}{A_L}$	$\frac{S_T}{S_L}$	$\frac{A_T}{A_L}$	$\frac{S_T}{S_L}$	$\frac{A_T}{A_L}$	$\frac{S_T}{S_L}$
$Le = 0.8$	1	1.62	1.61	1.69	1.68	3.5	3.47	3.26	3.23	5.33	5.29
	2	2.49	2.48	2.63	2.63	4.05	4.05	5.74	5.73	6.71	6.70
	4	2.64	2.62	2.36	2.35	2.69	2.67	2.32	2.30	1.50	1.48
	6	1.90	1.88	1.70	1.68	0.44	0.43	0.28	0.28	0.15	0.15
	8	0.94	0.93	1.07	1.06	0.04	0.04	0.03	0.03	0.02	0.02
	10	0.17	0.17	0.19	0.19	0.01	0.01	0.01	0.01	0.01	0.01
$Le = 1.0$	1	1.57	1.55	1.59	1.57	2.79	2.78	2.91	2.9	4.18	4.17
	2	1.67	1.66	1.6	1.59	2.99	2.99	3.95	3.93	4.77	4.76
	4	1.77	1.76	1.73	1.71	2.34	2.31	2.39	2.37	2.03	2.01
	6	1.64	1.62	1.68	1.66	1.43	1.41	0.74	0.74	0.68	0.67
	8	1.51	1.49	1.53	1.51	0.5	0.49	0.20	0.19	0.12	0.12
	10	0.86	0.85	0.85	0.84	0.09	0.09	0.03	0.03	0.03	0.03
$Le = 1.2$	1	1.29	1.28	1.22	1.21	1.92	1.91	2.04	2.02	2.68	2.66
	2	1.38	1.37	1.33	1.32	2.01	2.00	2.75	2.74	3.43	3.43
	4	1.31	1.30	1.28	1.27	1.82	1.81	1.98	1.96	1.57	1.55
	6	1.30	1.29	1.29	1.28	1.60	1.59	1.51	1.49	1.23	1.22
	8	1.23	1.22	1.24	1.23	1.12	1.11	0.60	0.60	0.47	0.46
	10	1.15	1.14	1.14	1.13	0.60	0.60	0.18	0.18	0.10	0.10

normal distance $u_\tau x_1/\nu$ of $T = (\hat{T}-T_0)/(T_{ad}-T_0) = 0.9$ isosurafce has been found to be about 15.0 for the quenching flames considered here.

4. Results & discussion

The instantaneous distributions of non-dimensional temperature $T = (\hat{T}-T_0)/(T_{ad}-T_0)$ at the central x_1–x_2 plane at different stages of flame quenching are shown in Fig. 2 for cases A-E. The cases B and D are not explicitly shown in the subsequent figures due to their qualitative similarities to cases A and E respectively (see Fig. 2). The statistics related to quenching distance and wall heat flux magnitude and distributions of T for cases A–E has been shown in Ref. [30] (interested readers are referred to Figs. 1, 2 and 3 of Ref. [30]), which revealed that cases B and D exhibit qualitatively similar trends as that of in cases A and E, respectively, which can also be seen from the temporal evolutions of turbulent flame speed and flame surface area in Table 2. A comparison between cases A, C and E provides an overview of flame-turbulence interaction for this database. The same approach was also adopted in previous publications without compromising the generality [30–35].

The extent of completion of chemical reaction and the species field in premixed flames can be quantified in terms of a reaction progress variable c, which is defined here in terms of a suitable reactant mass fraction Y_R as:

$$c = \frac{Y_{R0}-Y_R}{Y_{R0}-Y_{R\infty}} \tag{8}$$

where the subscripts 0 and ∞ refer to the values in the unburned and fully burned gases respectively. The reaction progress variable c increases monotonically from 0 to 1 from unburned reactants to fully burned products. The contours of $c = 0.1$–0.9 (from left to right) in steps of 0.2 are overlaid on the non-dimensional temperature field. It is worth noting that c is not equal to T for non-unity Lewis number (i.e. $Le \neq 1$) flames, and T can assume super-adiabatic values (i.e. $T > 1$) when the flame wrinkles are convex (concave) towards the reactants for $Le < 1$ ($Le > 1$) flames. This behaviour has been explained and discussed in detail elsewhere [30,51,57] and thus is not repeated here. In the case of head-on quenching the equality between c and T does not hold in the near-wall region irrespective of the value of Le because of the different boundary conditions for c (Neumann boundary condition) and T (Dirichlet boundary condition) at the wall [22,30–35]. All the flames are initially kept $20\delta_Z$ away from the wall, but the cases with high values of u'/S_L show early indications of flame quenching because in these cases flames are highly wrinkled and as a result these highly wrinkled flame fingers reach close to the wall relatively early and eventually quench. This tendency is more prevalent in the cases with smaller values of Le. The flames with $Le < 1$ show higher rate of flame propagation and greater extent of flame wrinkling away from the wall because in these cases reactants diffuse faster into the reaction zone than the rate at which heat diffuses out of it which in turn gives rise to higher rates of burning than the unity Lewis number case with statistically similar unburned gas turbulence due to simultaneous occurrence of high reactant concentration and high temperature. Just the opposite mechanism in the $Le > 1$ cases leads to smaller rate of burning than the unity Lewis number case with same unburned gas turbulence when the flame is away from the wall. Furthermore, in the $Le < 1$ cases, the regions with convex curvature towards the reactants experience a combination of strong focussing of reactants and weak defocussing of heat, which leads to an enhanced burning and flame wrinkling in these regions. By contrast, the combination of weak focussing of reactants and strong defocussing of heat leads to smaller extent of flame wrinkling in the $Le > 1$ cases than in the corresponding $Le = 1$ case when the flame is away from the wall. The aforementioned behaviour is consistent with several previous analyses [47–62,66,67]. The extent of burning and flame wrinkling can be quantified from normalised turbulent flame speed S_T/S_L and the normalised flame surface area A_T/A_L respectively where $S_T = (\rho_0 A_p)^{-1}\int_V \dot{\omega} dV$ and $A = \int_V |\nabla c| dV$ with $\dot{\omega}$ being the reaction rate of progress variable, A_p is the projected flame area in the direction of mean flame propagation, and the integration is performed over the whole volume. Table 2 lists the temporal evolutions of S_T/S_L and A_T/A_L for cases A-E. The flame wrinkles come in the vicinity at the wall and starts to quench at an earlier time instant for cases with higher rate of flame propagation and greater extent flame wrinkling and this trend strengthens with decreasing Le and increasing u'/S_L.

The spatial distributions of $u'/S_L = \sqrt{2\widetilde{k}/3}/S_L$ is shown in Fig. 3, which shows that relatively high values of $\sqrt{2\widetilde{k}/3}/S_L$ are obtained ahead of the flame, but they decrease across the flame brush and also in the vicinity of the isothermal inert wall. It can be seen that $\sqrt{2\widetilde{k}/3}/S_L$ decreases with time but it remains non-negligible at the time instants $t = 2\delta_Z/S_L$, $6\delta_Z/S_L$ and $10\delta_Z/S_L$. Thus, the following discussion for these time instants will represent different stages of turbulent flow topology distributions in the case of the head-on quenching of turbulent premixed flames.

The instantaneous distributions of $P^* = P \times (\delta_Z/S_L)$, $Q^* = Q \times (\delta_Z/S_L)^2$ and $R^* = R \times (\delta_Z/S_L)^3$ at different stages of quenching are shown for cases A, C and E in Figs. 4–6 respectively. A comparison between Figs. 2 and 4 reveals that high negative values of P^* are obtained within the flame (i.e. $0 < c < 1$) and P^* assumes vanishingly small values outside the flame in both unburned gases and fully burned products in the $Le = 1.0$ cases when the flame is away from the wall (i.e. before the quenching is initiated and thus this effect is prominent in case A because the flame started to quench by the time $t = 2\delta_Z/S_L$ in cases C and E). The inhomogeneity in the burned gas temperature is observed in non-unity Lewis number cases and this behaviour is particularly prevalent in the $Le = 0.8$ cases because of high rates of localised burning and relatively weak thermal diffusion rate. Thus, the effects of dilatation rate $\nabla\cdot\vec{u} = -P$ in the $Le = 0.8$ cases persist also in the burned gas beyond the flame, whereas these effects are weak in the $Le = 1.2$ cases. Moreover, it can be seen from Figs. 2 and 4 that comparatively high (small) magnitudes of P^* are obtained for the locations where the c-isosurfaces are concavely (convexly) curved towards the reactants. Focussing (defocussing) of heat at the concavely (convexly) curved zones gives rise to high positive (either small positive or negative) dilatation rate $(\partial u_i/\partial x_i) = -P$. Thus negative values of P^* with high

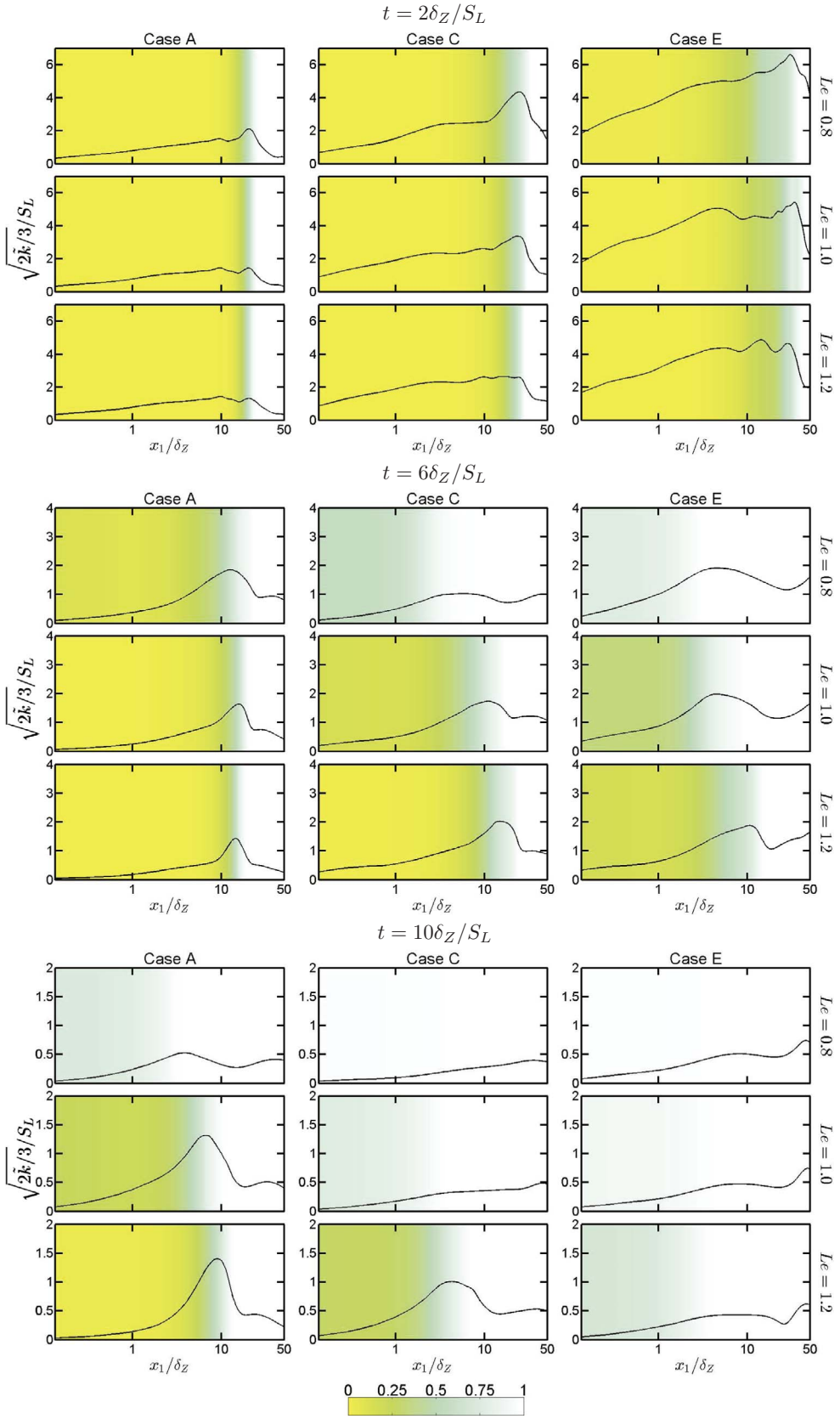

Fig. 3. Variation of $\sqrt{2\widetilde{k}/3}/S_L$ with x_1/δ_Z for cases A, C and E (1st–3rd column) at $t = 2\delta_Z/S_L$, $6\delta_Z/S_L$ and $10\delta_Z/S_L$ (1st–3rd row). For illustration purpose $\widetilde{c}$ is indicated by background colour in Figs. 3, 7,8,9,10, 15 and 16.

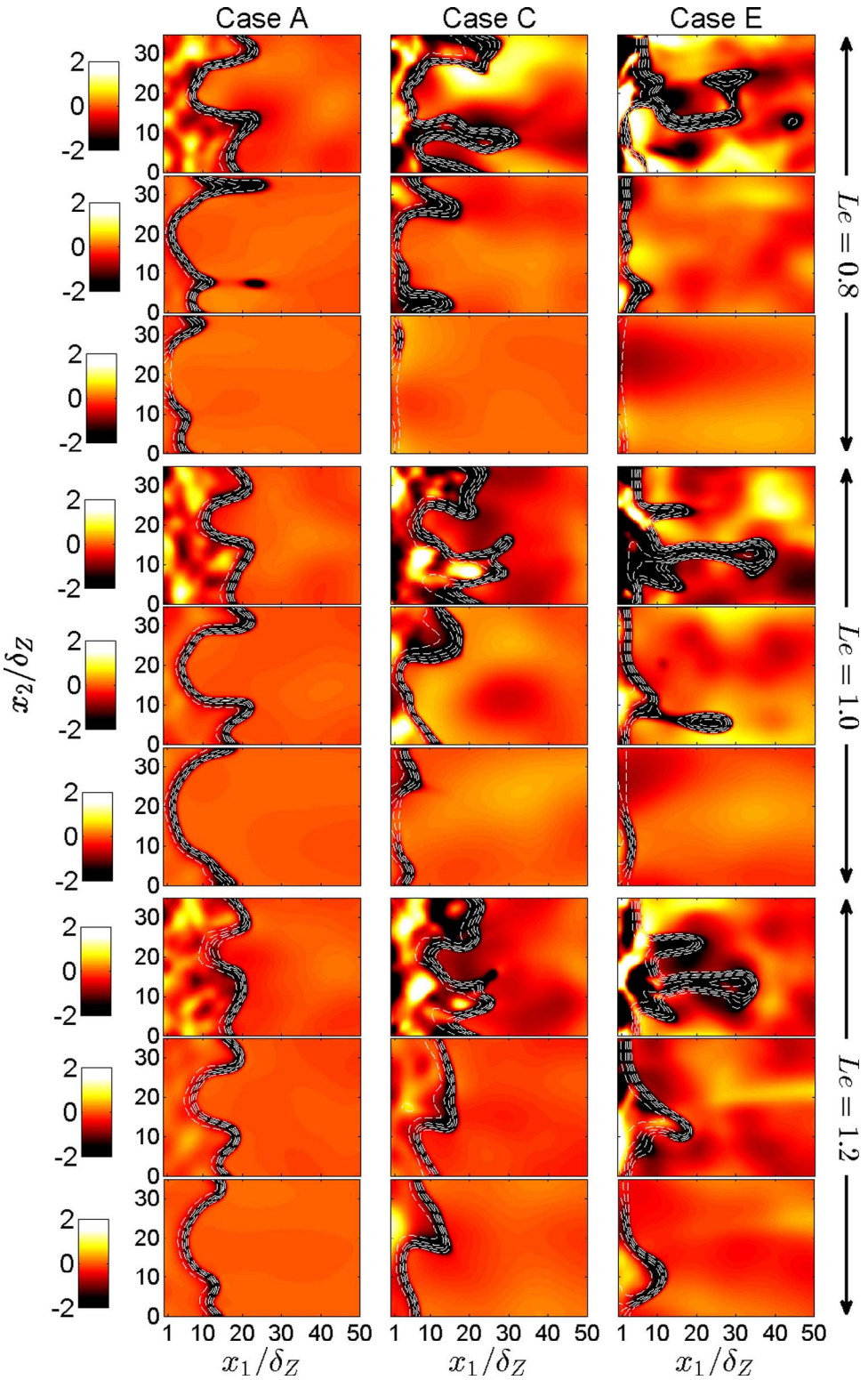

Fig. 4. Instantaneous $P^* = P \times \delta_Z/S_L$ fields for cases A, C and E (1st-3rd column) at $t = 2\delta_Z/S_L$, $4\delta_Z/S_L$ and $6\delta_Z/S_L$ (1st–3rd row), white lines are c-isolines from 0.1 to 0.9 in steps of 0.2.

magnitude are obtained in the regions which are concavely curved towards the reactants, whereas either small negative or positive values of P^* are observed for the locations which are convex towards the reactants. Furthermore, it can be seen from Fig. 4 that the likelihood of obtaining high magnitude of P^* drops significantly with time as quenching progresses which leads to the weakening of the effects of thermal expansion.

The expression for the third invariant R in Eq. (4) can be recast as:

$$R = \frac{1}{3}(-P^3 + 3PQ - S_{ij}S_{jk}S_{ki}) - \frac{1}{4}\omega_i S_{ij}\omega_j = \underbrace{\frac{1}{3}(-P^3 + 3PQ_S - S_{ij}S_{jk}S_{ki})}_{R_S} + PQ_W - \frac{1}{4}\omega_i S_{ij}\omega_j \quad (9)$$

where R_S is the third invariant of the strain rate $S_{ij} = 0.5\,(\partial u_i/\partial x_j + \partial u_j/\partial x_i)$ tensor. Eq. (9) suggests that $R^* = R \times (\delta_Z/S_L)^3$ may assume high positive or negative values where there is an imbalance

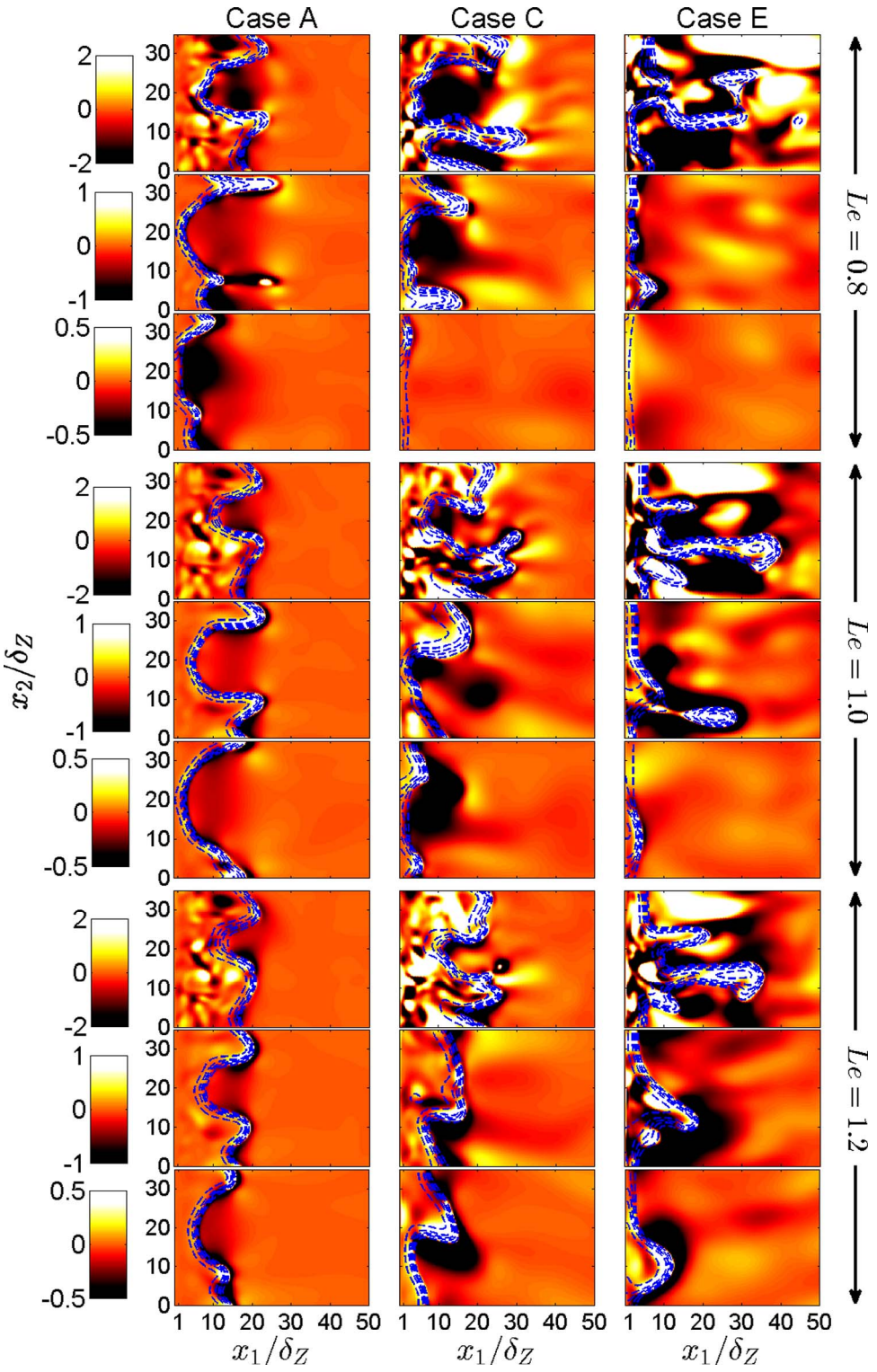

Fig. 5. Instantaneous $Q^* = Q \times (\delta_Z/S_L)^2$ fields for cases A, C and E (1st–3rd column) at $t = 2\delta_Z/S_L$, $4\delta_Z/S_L$ and $6\delta_Z/S_L$ (1st–3rd row), blue lines are c-isolines from 0.1 to 0.9 in steps of 0.2.

between R_S and $PQ_W - \frac{1}{4}\omega_i S_{ij}\omega_j$. This imbalance is pronounced on both the unburned gas side and within the flame and both positive and negative values of R^* are observed. The magnitude of R^* drops sharply across the flame for the $Le = 1.0$ and 1.2 cases (see Figs. 2 and 6). A comparison between Figs. 2 and 6 reveals that R^* assumes significant magnitude not only in the unburned gas and within the flame, but also in the burned gas due to appreciable presence of dilatation rate $\nabla\cdot\vec{u} = -P$ in the burned gas (see P dependence of R in Eq. (9)) in the $Le = 0.8$ cases. The likelihood of obtaining high magnitudes of R^* increases with increasing (decreasing) u'/S_L (Le) and $|R^*|$ decreases as quenching progresses with time.

The variations of normalised mean value of the first invariant $\langle P^*\rangle$ (where $\langle q\rangle = 1/(L_2L_3)\int_0^{L_3}\int_0^{L_2} q dx_2 dx_3$ for a general quantity q) with wall normal distance are shown in Fig. 7 for cases A, C and E at different time instants. It can be seen from Fig. 7 that $\langle P^*\rangle$ remains predominantly negative values because of overwhelmingly positive values of dilatation rate in premixed turbulent flames (see high likelihood of obtaining negative value of P^* in Fig. 4). However, the magnitude of the negative mean value of P^* decreases with time as the quenching progresses. The

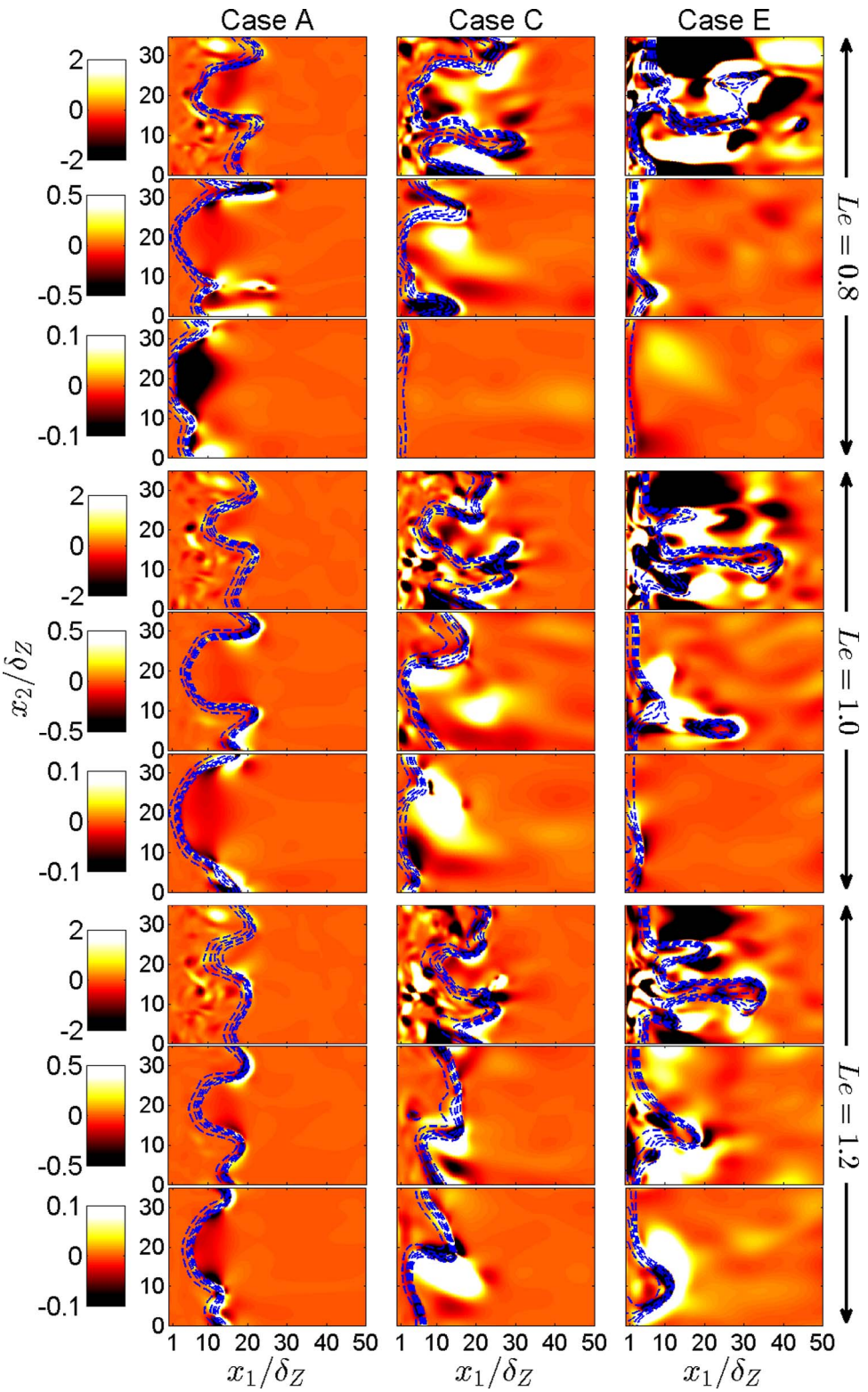

Fig. 6. Instantaneous $R^* = R \times (\delta_Z/S_L)^3$ fields for cases A, C and E (1st-3rd column) at $t = 2\delta_Z/S_L$, $4\delta_Z/S_L$ and $6\delta_Z/S_L$ (1st–3rd row), blue lines are c-isolines from 0.1 to 0.9 in steps of 0.2.

effects of heat release weaken as quenching progresses which reduce the magnitude of positive dilatation rate. It is worth noting that turbulence severely decays in the burned gas and $\partial u_i/\partial x_i$ becomes negative close to the wall due to the flow reversal at the late stages of flame quenching which leads to positive value of $\langle P^* \rangle$ at later times.

The variation of $\langle Q^* \rangle = \langle Q \rangle \times (\delta_Z/S_L)^2$, and its components, $\{\langle Q_S \rangle, \langle Q_W \rangle\} \times (\delta_Z/S_L)^2$, with normalised wall normal distance x_1/δ_Z for cases A, C and E are shown in Fig. 8 for different time instants. Eq. (3) suggests that $\nabla \cdot \vec{u} = -P$ and $\sqrt{S_{ij}S_{ij}}$ affect $Q_S = (P^2 - S_{ij}S_{ij})/2$, whereas the component $Q_W = W_{ij}W_{ij}/2$ depends on enstrophy Ω (i.e. $W_{ij}W_{ij}/2 = \omega_i\omega_i/4 = \Omega/2$ where ω_i is the ith component of vorticity). The contribution of $\langle Q_W \rangle$ is deterministically positive and it is evident from Fig. 8 that $\langle Q_W \rangle$ assumes high values of at the wall but also increases within the flame due to flame generated vorticity due to baroclinic

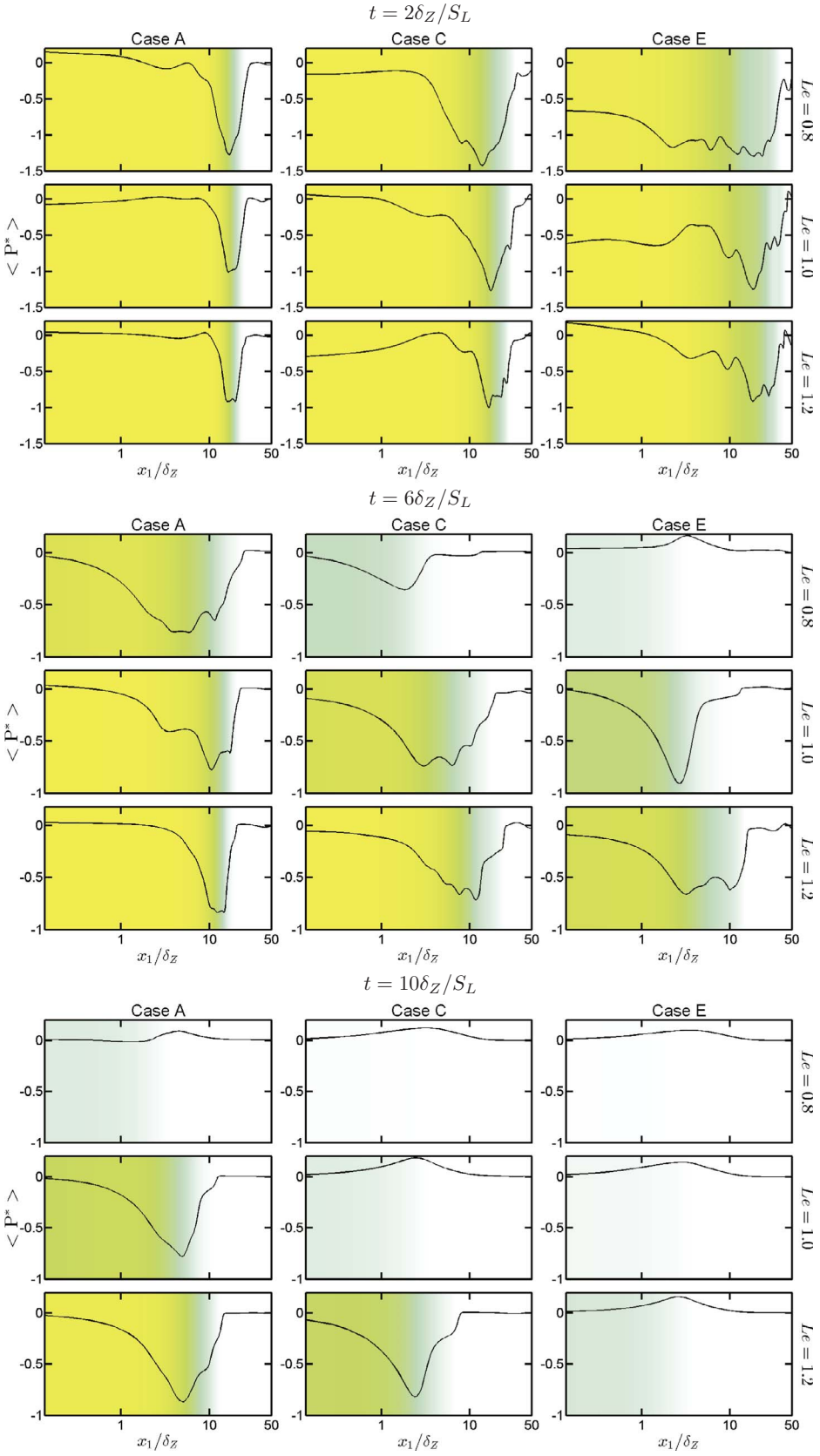

Fig. 7. Variations of $\langle P^* \rangle = \langle P \rangle \times \delta_Z/S_L$ with x_1/δ_Z for $t = 2\delta_Z/S_L$, $6\delta_Z/S_L$, $10\delta_Z/S_L$.

torque. Interested readers are referred to Ref. [35] for more discussion on vorticity and enstrophy transport in the near-wall region in this configuration for these cases.

The sign of $\langle Q_S \rangle = \langle P^2 - S_{ij}S_{ij} \rangle/2$ depends on the relative magnitudes of $\langle P^2 \rangle$ and $\langle S_{ij}S_{ij} \rangle$. It can be seen from Fig. 8 that $\langle Q_S \rangle$ predominantly assumes negative values and assumes locally small positive values away

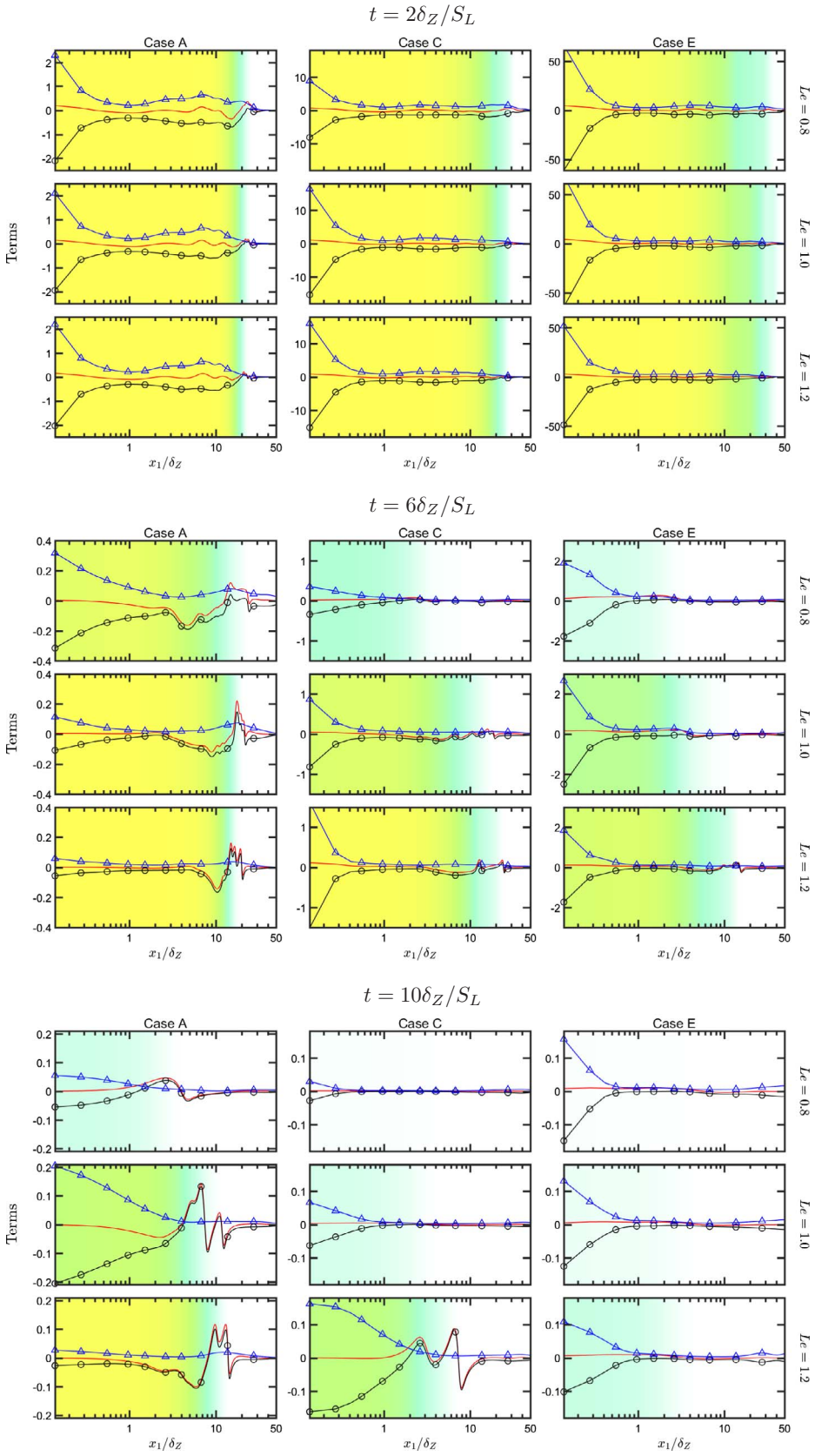

Fig. 8. Variations of normalised terms {⟨Q⟩ (——), ⟨Q_S⟩ (—○—), ⟨Q_W⟩ (—△—)} × $(\delta_Z/S_L)^2$ with x_1/δ_Z for $t = 2\delta_Z/S_L$, $6\delta_Z/S_L$, $10\delta_Z/S_L$.

from the wall within the flame where $\langle P^2\rangle/2$ dominates over $\langle -S_{ij}S_{ij}\rangle/2$. The effects of dilatation rate $\nabla\cdot\vec{u} = -P$ remains weak close to the wall and thus $\langle -S_{ij}S_{ij}\rangle/2$ dominates over $\langle P^2\rangle/2$ to lead to a negative value of $\langle Q_S\rangle$. The magnitude of $\langle S_{ij}S_{ij}\rangle/2$ decreases within the flame whereas $\langle P^2\rangle/2$ increases in reaction zone, so $\langle P^2\rangle/2$ is likely to overcome $\langle -S_{ij}S_{ij}\rangle/2$ in this region and yield a positive value of $\langle Q_S\rangle$. The quantity

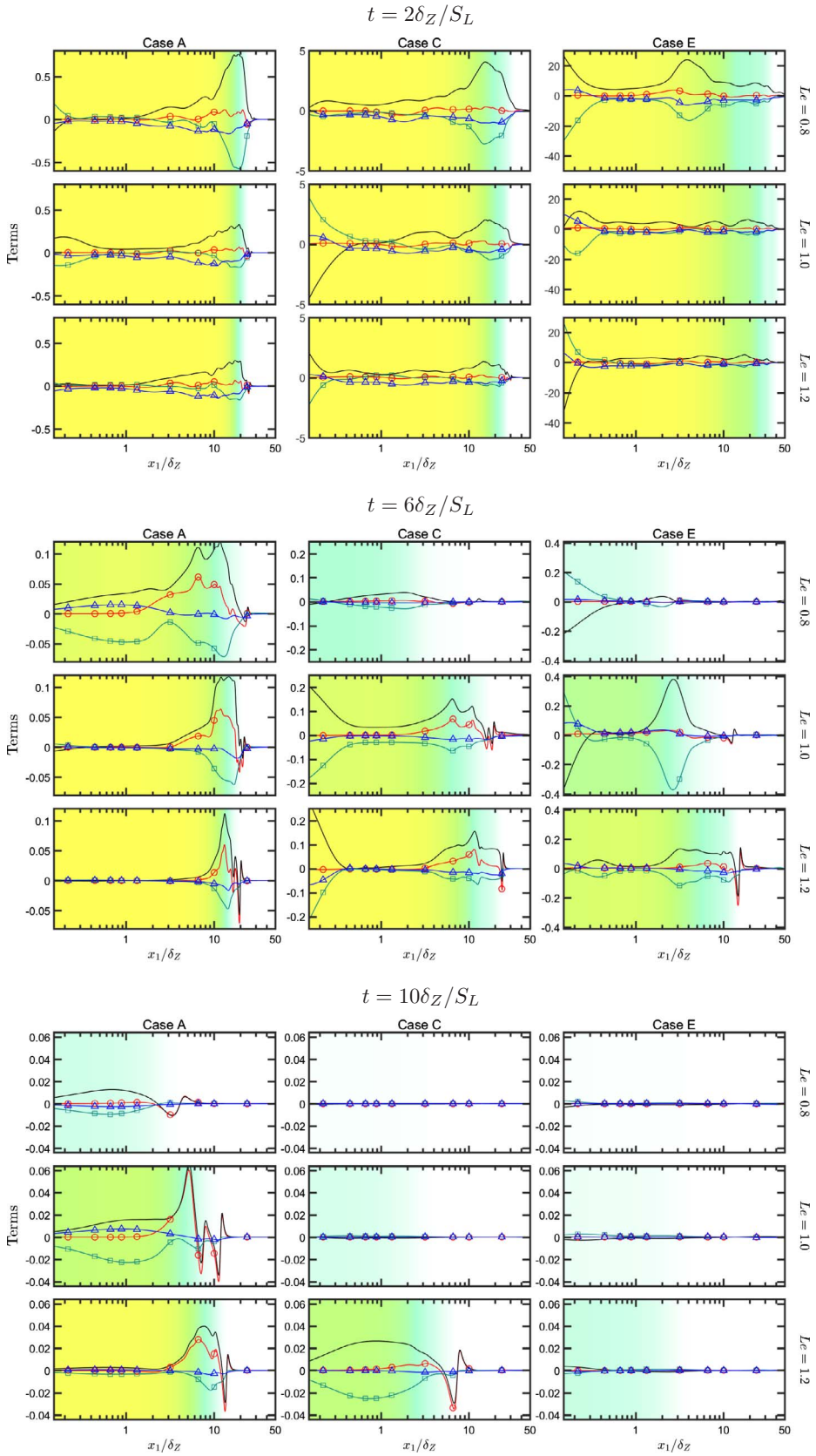

Fig. 9. Variations of normalised terms { $\langle R \rangle$ (—○—), $\langle R_S \rangle$ (——), $\langle PQ_W \rangle$ (—□—), $\langle -\omega_i S_{ij} \omega_j/4 \rangle$ (—△—) } × $(\delta_Z/S_L)^3$ with x_1/δ_Z for $t = 2\delta_Z/S_L$, $6\delta_Z/S_L$, $10\delta_Z/S_L$.

$\langle Q_S \rangle$ can be expressed as: $\langle Q_S \rangle = \langle Q_{S1} \rangle + \langle Q_{S2} \rangle = \langle P^2/3 \rangle - \langle E/4\nu \rangle$ with $E = (\tau_{ij}\partial u_i/\partial x_j)/\rho$ and ν being the dissipation rate of instantaneous kinetic energy (i.e. $u_i u_i/2$) and kinematic viscosity respectively. Thus, $\langle Q_S \rangle > 0$ ($\langle Q_S \rangle < 0$) corresponds to dilatation (dissipation) dominated regions. Wacks et al. [21] demonstrated that one obtains $Q_{S1}/|Q_{S2}| \sim \tau^2 Ka^{-2}$, using $Q_{s1} = P^2/3 \sim \{\tau S_L/\delta_{th}\}^2$ [21,60,61] and

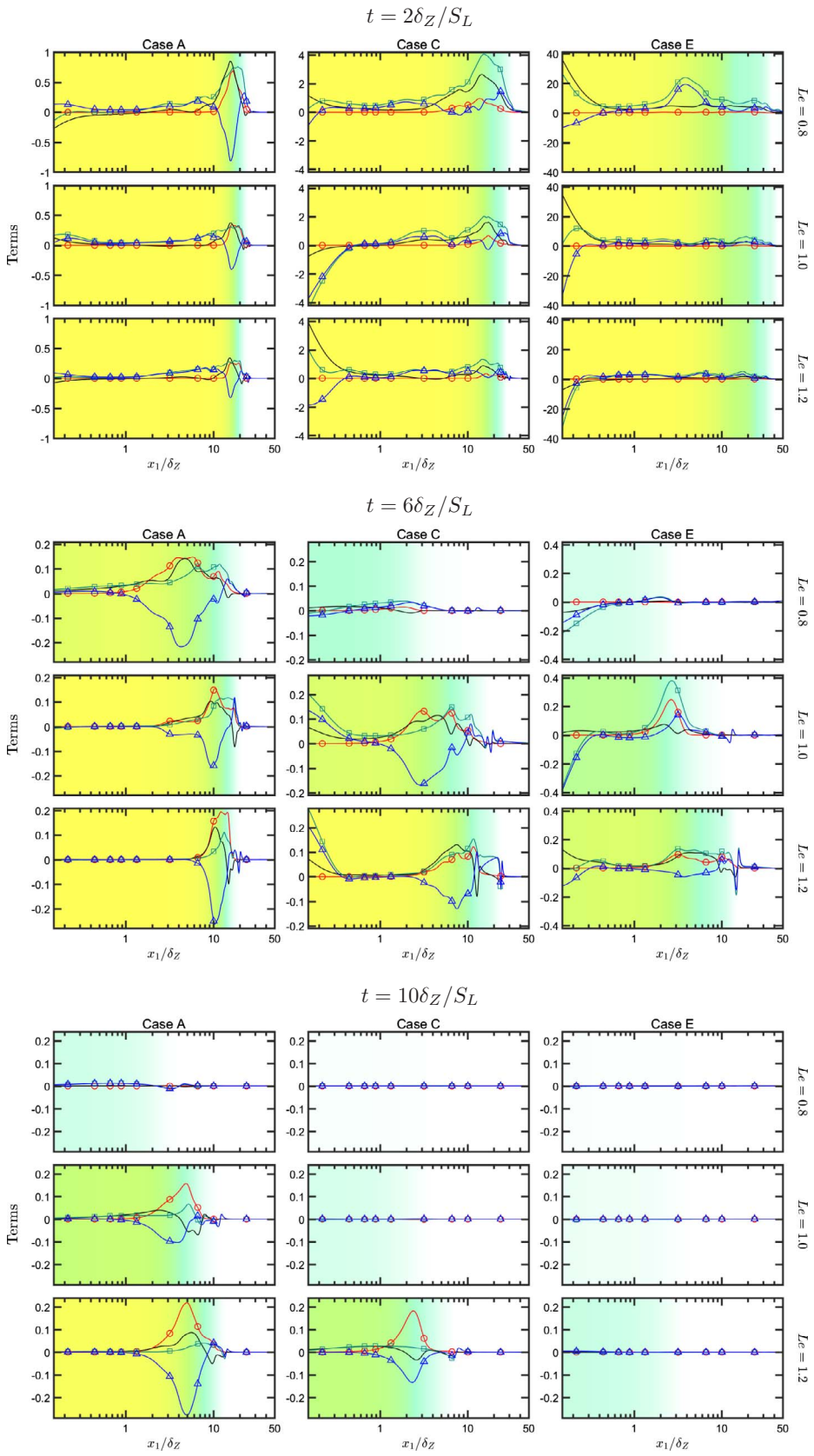

Fig. 10. Variations of normalised terms $\{\langle R_S\rangle$ (—□—), $\langle -P^3/3\rangle$ (—○—), $\langle PQ_S\rangle$ (——), $\langle -S_{ij}S_{jk}S_{ki}/3\rangle$ (—△—)$\} \times (\delta_Z/S_L)^3$ with x_1/δ_Z for $t = 2\delta_Z/S_L, 6\delta_Z/S_L, 10\delta_Z/S_L$.

$|Q_{S2}| = |-E/4\nu| \sim 1/\tau_\eta^2$ with τ_η being the Kolmogorov time scale. For all cases considered here $Ka \gg 1$ and thus $|\langle Q_{S2}\rangle|$ dominates over $\langle Q_{S1}\rangle$ to yield predominantly negative value of $\langle Q_S\rangle$.

In all cases $\langle Q_S\rangle$ and $\langle Q_W\rangle$ mostly balance each other and as a result the magnitude of $\langle Q\rangle$ remains negligible in comparison to those of $\langle Q_S\rangle$ and $\langle Q_W\rangle$. The magnitudes of $\langle Q_S\rangle$ and $\langle Q_W\rangle$ are greater for higher

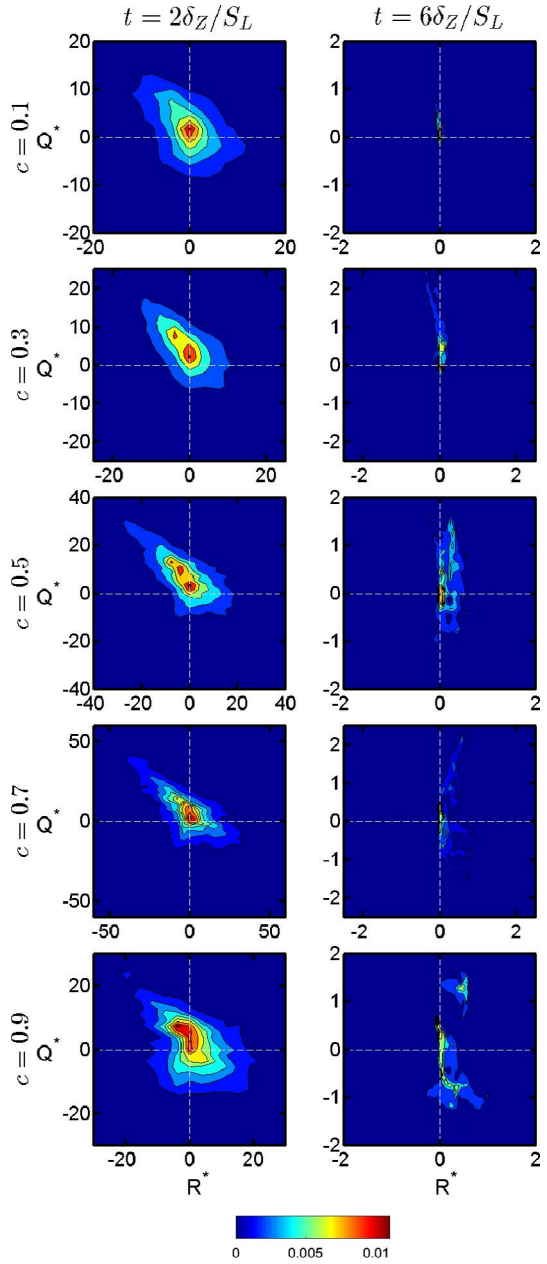

Fig. 11. Joint PDFs of $Q^* = Q \times (\delta_Z/S_L)^2$ and $R^* = R \times (\delta_Z/S_L)^3$ on c−isosurfaces c = 0.1,0.3,0.5,0.7,0.9 for $t = 2\delta_Z/S_L$ and $6\delta_Z/S_L$ with case E and Le = 1.0.

values of u'/S_L for a given value of Le. On the other hand both $\langle Q_S \rangle$ and $\langle Q_W \rangle$ assume higher magnitudes for the cases with smaller values of Le for a given value of u'/S_L. The magnitudes of $\langle Q \rangle$,$\langle Q_S \rangle$ and $\langle Q_W \rangle$ decay with time as quenching progresses.

The variation of $\langle R^* \rangle = \langle R \rangle \times (\delta_Z/S_L)^3$, and its components, $\{\langle R_S \rangle$,$\langle PQ_W \rangle$,$-\langle \omega_i S_{ij} \omega_j/4 \rangle\} \times (\delta_Z/S_L)^3$, with normalised wall normal distance x_1/δ_Z for cases A, C and E are shown in Fig. 9 for different time instants. It can be seen from Eq. (9 that $R_S = (-P^3 + 3PQ_S - S_{ij}S_{jk}S_{ki})/3$ contains a contribution to the strain rate transport (i.e. $-S_{ij}S_{jk}S_{ki}$), whereas $(PQ_W - \omega_i S_{ij} \omega_j/4)$ is related the enstrophy transport [18–21]. It is possible to approximate $R_S \approx -S_{ij}S_{jk}S_{ki}/3 > 0$ and $PQ_W - \omega_i S_{ij} \omega_j/4 \approx -\omega_i S_{ij} \omega_j/4 < 0$ away from the flame front, where $P \approx 0$, hence, R^* may assume high positive or negative values where there is an imbalance of $(-S_{ij}S_{jk}S_{ki}/3)$ and $(-\omega_i S_{ij} \omega_j/4)$ away from the flame [18–21]. The contributions of $\langle PQ_W - (\omega_i S_{ij} \omega_j)/4 \rangle$ and $\langle R_S \rangle$ appear to balance across the flame front in all cases (see Fig. 9).

Finally, Fig. 10 shows the variation of the normalised values of the components $\langle R_S \rangle \times (\delta_Z/S_L)^3$: $\{-\langle P^3/3 \rangle$,$\langle PQ_S \rangle$,$\langle -S_{ij}S_{jk}S_{ki}/3 \rangle\} \times (\delta_Z/S_L)^3$ with normalised wall normal distance x_1/δ_Z for cases A, C and E for different time instants. In all cases $-\langle P^3/3 \rangle$ assumes predominantly positive values within the flame due to overwhelming probability of obtaining negative values of P when the flame remains away from the wall. However, the magnitude of $-\langle P^3/3 \rangle$ decreases significantly as the quenching progresses. The predominantly negative values of P and Q_S (see Figs. 7 and 9) give rise to predominantly positive values of $\langle PQ_S \rangle$. However, it has been mentioned earlier that Q_S can assume positive within the flame where $P^2/2$ overcomes $-S_{ij}S_{ij}/2$, which acts to promote negative values of $\langle PQ_S \rangle$. The magnitude of $\langle PQ_S \rangle$ decreases as time progresses due to the decays of the magnitudes of P and Q_S. The behaviour of the contribution of $\langle -S_{ij}S_{jk}S_{ki}/3 \rangle$ shows dependence on turbulence intensity u'/S_L and global Lewis number Le at early times (e.g. $t = 2\delta_Z/S_L$). For example, $\langle -S_{ij}S_{jk}S_{ki}/3 \rangle$ shows large negative values within the flame front for case A, whereas positive values of $\langle -S_{ij}S_{jk}S_{ki}/3 \rangle$ within the flame front have been found for cases C and E. The magnitude of positive contribution of $\langle -S_{ij}S_{jk}S_{ki}/3 \rangle$ within the flame front decreases with increasing Le.

The contours of joint pdf between Q^* and R^* for case E with Le = 1.0 are exemplarily shown in Fig. 11 for c = 0.1,0.3,0.5,0.7 and 0.9 at $t = 2\delta_Z/S_L$ and $6\delta_Z/S_L$. The other cases are not shown because the qualitative behaviour of this joint pdf does not change with the variations of u'/S_L and Le. Values of these joint PDFs are of limited value for Fig. 11 because the whole point of these plots is to compare the nature of the correlation between Q^* and R^* across the flame front. A dominant negative correlation between Q^* and R^* has been observed within the flame front when the flame remains away from the wall. However, this negative correlation between Q^* and R^* weakens as time progresses and the flame approaches the wall. At $t = 6\delta_Z/S_L$ the joint pdf between Q^* and R^* exhibits weak negative correlation towards the unburned gas side and these quantities do not show any appreciable correlation as c increases towards the burned gas side.

Fig. 12 shows the variations of the volume fractions VF of individual flow topologies $S1$−$S8$ conditional on c across the flame front (over the range $0.01 \leq c \leq 0.99$) for cases A, C and E for Le = 0.8,1.0 and 1.2 at different time instants. It is worth noting that the range of c obtained at a given instant of time changes as the quenching progresses (see Fig. 2 and also temporal evolution of the probability density function of c in [30,31]) and the probability of obtaining $c \approx 1.0$ increases as the time elapses. A similar presentation of volume fraction of individual flow topologies was used by Cifuentes and his co-workers [18,19]. It can be seen from Fig. 12 that the volume fractions VF of all topologies remain significant within the flame except for $S5$ and $S6$ when the flames are away from the wall, which is consistent with previous analyses [18,19]. Strong thermal expansion within the flame leads to strongly negative values of P (i.e. high positive values of dilatation rate $\nabla \cdot \vec{u}$), which implies that the occurrence of $P > 0$ topologies (i.e. $S5$ and $S6$) is greatly disadvantaged. Fig. 4 shows sporadic existences of $P > 0$ in the burned gas region for non-unity Lewis number flames and also for unity Lewis number flames once the quenching is initiated. These positive P locations ultimately give rise to finite probabilities of finding $S5$ and $S6$ topologies towards the burned gas side, but VF of $S5$ remains much higher than that of $S6$ in the burned gas region ($\widetilde{c} \rightarrow 1.0$). However, the volume fractions of $S5$ and $S6$ topologies increase significantly as flame quenching progresses with time. The mean flow reverses its direction from away from the wall to towards the wall and this behaviour leads to $P > 0$ at the final stages of quenching. The topologies $S7$ and $S8$ are typical of positive values of dilatation rate $\nabla \cdot \vec{u}$ (i.e. negative values of P) and it can be seen from Fig. 12 that the volume fraction of $S7$ topology remains a significant contributor within the flame front, and the probability of obtaining $S7$ topology increases with decreasing (increasing) Le (u'/S_L) when the flame is away from the wall. The extent of flame wrinkling increases with decreasing Le, and with increasing u'/S_L, and this gives rise to greater likelihood of finding high magnitudes of positive and negative curvatures. Accordingly, dilatation rate can

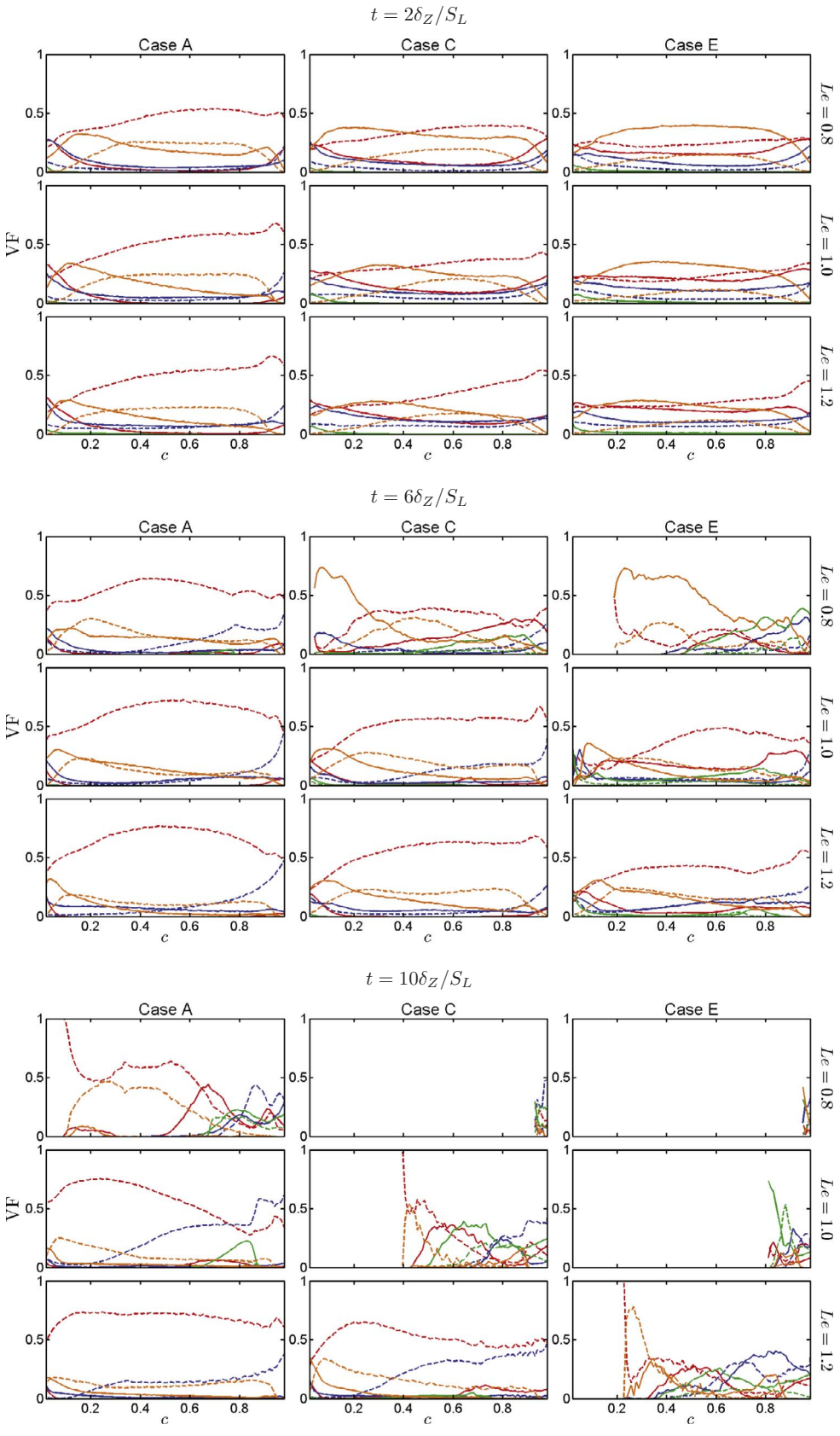

Fig. 12. Variations of volume fractions VF for topologies: Focal topologies S1 (——), S4 (——), S5 (——), S7 (——), nodal topologies S2 (— —), S3 (— —), S6 (— —), S8 (— —) with c for $t = 2\delta_Z/S_L, 6\delta_Z/S_L, 10\delta_Z/S_L$ for cases A, C and E with $Le = 0.8, 1.0$ and 1.2.

assume high positive values at the strongly negatively curved zones due to focussing of heat in these highly wrinkled regions. This increases the likelihood of finding negative values of P with high magnitude (i.e. high positive values of dilatation rate $\nabla\cdot\vec{u}$), which in turn results in a greater volume fraction of $S7$ within the flame front. The volume fractions of $S7$ and $S8$ decrease towards the burned gas side of the flame with the weakening of the effects of positive dilatation rate. The volume fractions of $S3$ and $S4$ topologies increase towards the burned gas side for

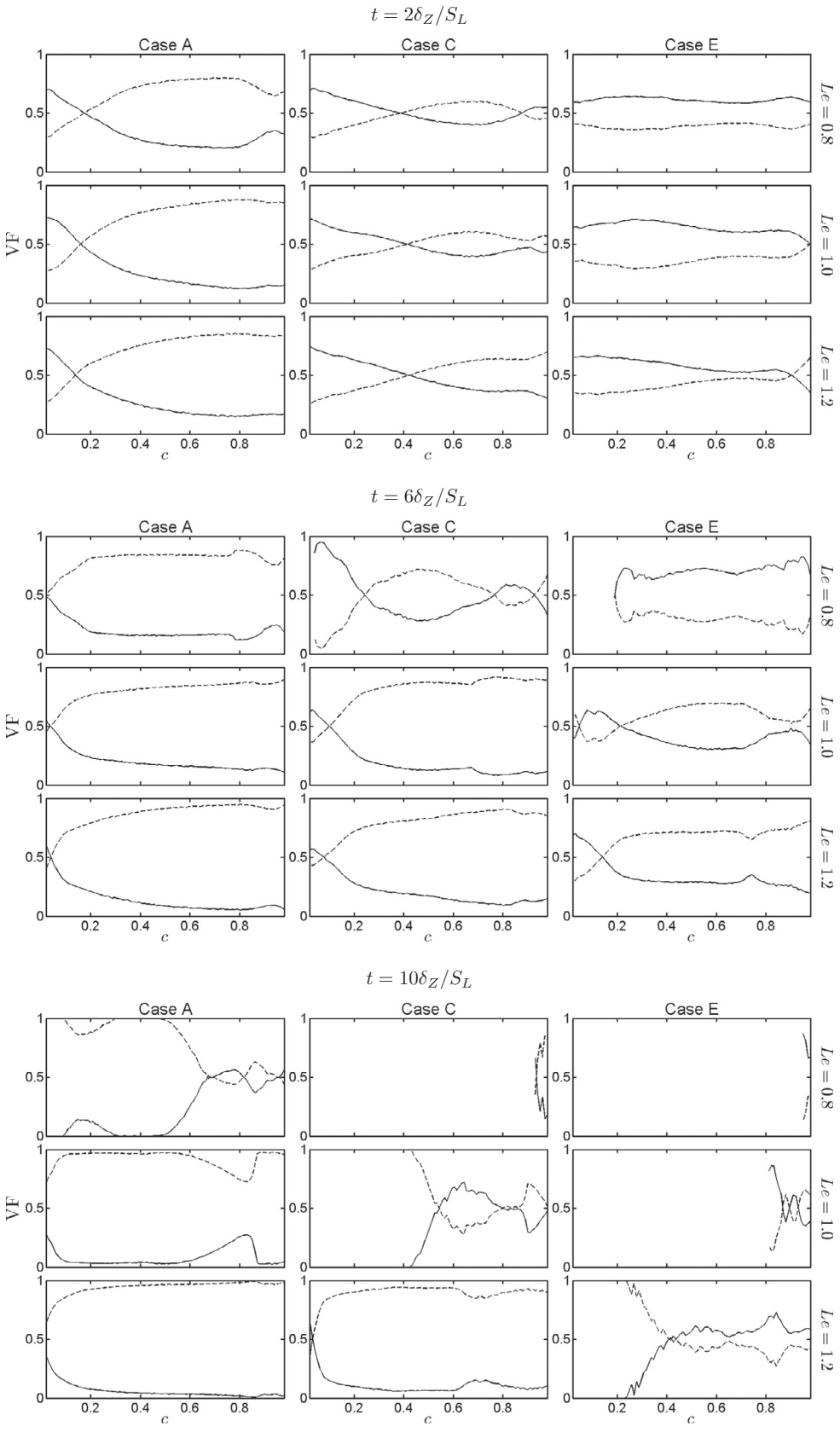

Fig. 13. Variations of volume fractions VF for focal (——) and nodal (— —) topologies with c for $t = 2\delta_Z/S_L, 6\delta_Z/S_L, 10\delta_Z/S_L$ for cases A, C and E with $Le = 0.8, 1.0$ and 1.2.

all cases even when the flame quenches. Especially the relative contribution of $S3$ volume fraction increases as the quenching progresses with time. The volume fraction of $S2$ topology assumes high value within the flame throughout the duration of head-on quenching. The volume fraction of $S1$ topology assumes significant values towards the burned gas side and its volume fraction decreases in the unburned gas. As the topologies $S1$,$S2$,$S3$ and $S4$ are present irrespective of the value of P, the probability of finding these topologies remain significant in all

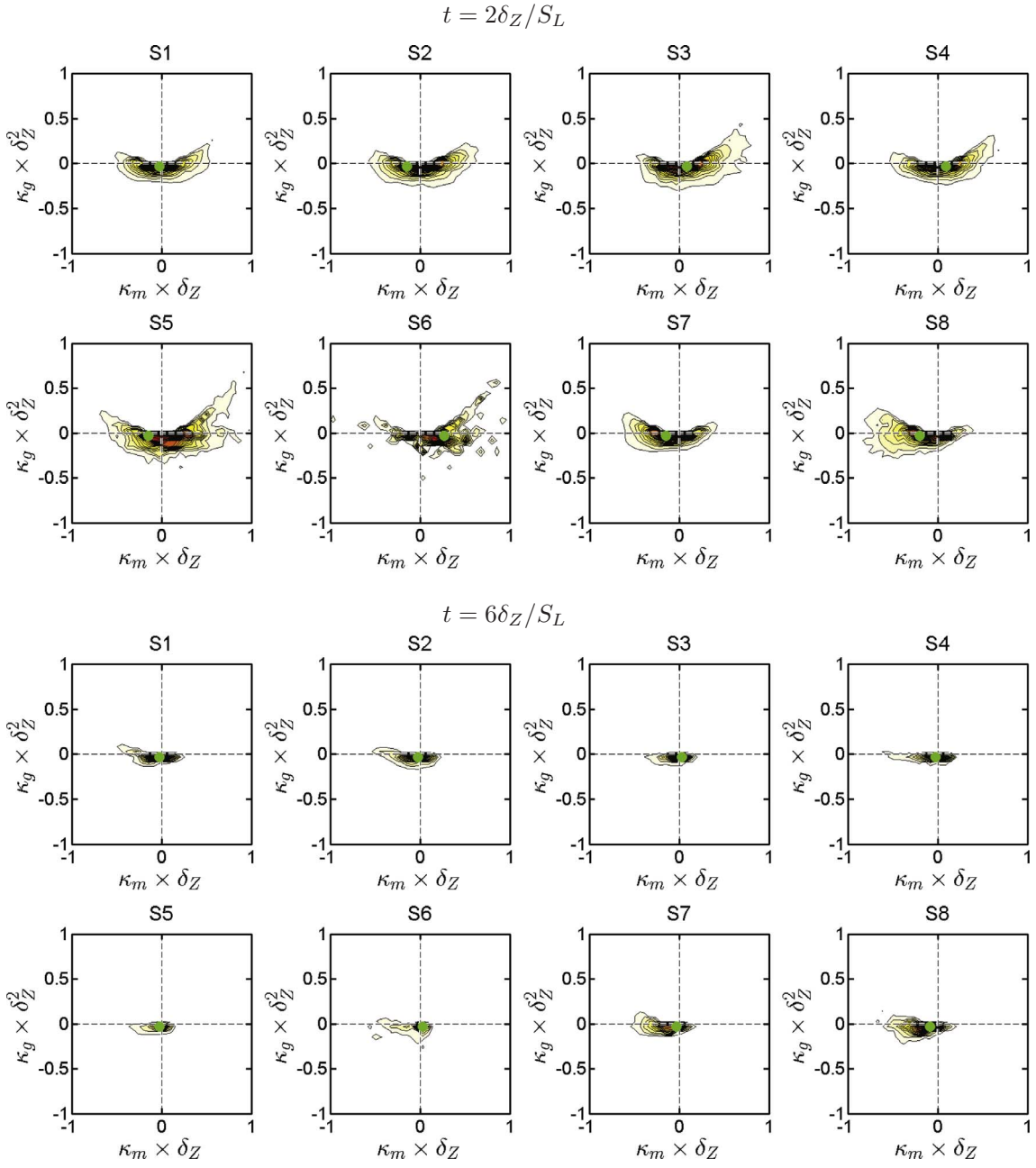

Fig. 14. Joint PDF between mean and Gaussian curvatures (i.e. $\kappa_m \times \delta_Z$ and $\kappa_g \times \delta_Z^2$) for S1–8 at $t = 2\delta_Z/S_L$ and $6\delta_Z/S_L$ for cases E with $Le = 1.0$.

cases at all stages of flame quenching.

The distributions of volume fractions of focal (*S*1,*S*4,*S*5,*S*7) and nodal (*S*2,*S*3,*S*6,*S*8) topologies conditional on *c* for cases A, C and E are shown in Fig. 13 for $Le = 0.8$,1.0 and 1.2. In general, the volume fraction of focal topologies decreases from the unburned to the burned gas side of the flame which is consistent with the decay of enstrophy across the flame brush in these cases (see Ref. [35]). This behaviour is also consistent with previous findings by Cifuentes and his co-workers [18,19]. The decrease (increase) in volume fraction of focal (nodal) topologies across the flame front is relatively less prominent in high values of u'/S_L. The likelihood of obtaining nodal and focal topologies are almost equally probable towards the unburned gas side of the flame front as the quenching progresses which implies that the volume fractions of nodal and focal topologies remain comparable at the wall where the unburned gas is confined at the final stage of quenching. Both global Lewis number *Le* and turbulence intensity u'/S_L have noticeable effects on the distributions of nodal and focal topologies. The focal topologies remain dominant in case E with $Le = 0.8$ when the flame is away from the wall and also during flame quenching, but case E with $Le = 1.0$ and 1.2 shows a monotonic decay (increase) of volume fractions of focal (nodal) topologies with increasing *c*. In summary, an increase (a decrease) in u'/S_L (*Le*) promotes focal topologies when the flame is away from the wall, but the probability of obtaining nodal (focal) topologies increases (decreases) as quenching progresses.

The interaction of flow and flame topologies is of fundamental importance in flame-turbulence interaction. According to Dopazo et al. [10] the flame topology can be described in terms of its mean and Gauss curvatures, κ_m and κ_g, respectively, where $\kappa_m = (\kappa_1 + \kappa_2)/2 = 1/2\nabla\cdot(-\nabla c/|\nabla c|)$ and $\kappa_g = \kappa_1\kappa_2$, in which κ_1 and κ_2 are the principal curvatures. It is worth noting that the region $\kappa_g > \kappa_m^2$ in the κ_m–κ_g plane, indicates complex curvatures and thus is non-physical. According to the present convention, positive (i.e. $\kappa_m > 0$) curvature is associated with the wrinkles which are convex to the reactants, whereas negative (i.e. $\kappa_m < 0$) curvature represents wrinkles which are concave

to the reactants. The combination of $\kappa_m > 0$ ($\kappa_m < 0$) and $\kappa_g > 0$ indicates cup convex (cup concave) flame topology, whereas the combination of $\kappa_m > 0$ ($\kappa_m < 0$) and $\kappa_g < 0$ represents saddle convex (saddle concave) flame topology. The combination of $\kappa_m > 0$ ($\kappa_m < 0$) and $\kappa_g = 0$ represents tile convex (tile concave) flame topology. Fig. 14 shows joint PDFs between the mean and Gauss curvatures (i.e. κ_m and κ_g) for cases A, C and E at $t = 2\delta_Z/S_L$ and $6\delta_Z/S_L$ for $Le = 1.0$ where the plots are coloured to highlight the relative values of the joint PDFs. The joint PDF value is of little use for these plots, and thus are not shown here. It is the shape of the distribution and its relative spread which hold useful information. The other cases are not explicitly shown because of their qualitative similarity to the scatter shown in Fig. 14. It can be seen from Fig. 14 that the distribution of $S1$ and $S2$ topologies are almost symmetrical about $\kappa_m = 0$, whereas $S7$ and $S8$ topologies appear to slightly favour $\kappa_m < 0$ and $\kappa_g > 0$ and $S5$ and $S6$ appear to slightly favour $\kappa_m, \kappa_g > 0$ when the flame is away from the wall (e.g. $t = 2\delta_Z/S_L$). The $S7$ and $S8$ topologies are associated with high positive dilatation rates (i.e. negative values of P) which are likely to be observed in the zones which are concavely curved towards the reactants (i.e. $\kappa_m < 0$) due to focussing of heat. By contrast, $S5$ and $S6$ topologies are associated with negative dilatation rates (i.e. positive values of P) which are likely to be observed in the zones which are convexly curved towards the reactants (i.e. $\kappa_m > 0$) due to defocussing of heat. Thus, the topologies $S7$ and $S8$ ($S5$ and $S6$) show a preference to $\kappa_m < 0$ ($\kappa_m > 0$) and $\kappa_g > 0$. As the flame quenching progresses with time, the joint PDF between κ_m and κ_g plane remains concentrated around the origin (see $t = 6\delta_Z/S_L$), but even so $S7$ and $S8$ topologies continue to show a preference towards $\kappa_m < 0$ and $\kappa_g > 0$.

It is worth noting that each of the flow topologies are associated with different types of generic flow structures. Thus, it is worth investigating the alignments of ∇c and vorticity $\vec{\omega}$ with local principal strain rates for individual topologies so that the contributions of these topologies to the scalar dissipation rate (SDR), $N_c = D\nabla c \cdot \nabla c$ (where D is the thermal diffusivity), and enstrophy $\Omega = \vec{\omega}\cdot\vec{\omega}/2$ transports in turbulent premixed flames can be understood. The transport equations of N_c and Ω are given as [9,35,60,67–69]:

$$\rho\frac{DN_c}{Dt} = \frac{\partial}{\partial x_j}\left(\rho D\frac{\partial N_c}{\partial x_j}\right) - 2D\frac{Dc}{Dt}\frac{\partial c}{\partial x_k}\frac{\partial \rho}{\partial x_k} - 2\rho D\underbrace{\frac{\partial c}{\partial x_i}\frac{\partial u_i}{\partial x_j}\frac{\partial c}{\partial x_j}}_{\Lambda} + 2D\frac{\partial \dot{\omega}}{\partial x_k}\frac{\partial c}{\partial x_k} - 2\rho D^2\frac{\partial^2 c}{\partial x_k \partial x_i}\frac{\partial^2 c}{\partial x_k \partial x_i} + f(D) \quad (10a)$$

$$\frac{D\Omega}{Dt} = \underbrace{\omega_i\omega_k\frac{\partial u_i}{\partial x_k}}_{V} - \epsilon_{ijk}\,\omega_i\frac{1}{\rho^2}\frac{\partial \rho}{\partial x_j}\frac{\partial \tau_{kl}}{\partial x_l} + \frac{\epsilon_{ijk}\,\omega_i}{\rho}\frac{\partial^2 \tau_{kl}}{\partial x_j \partial x_l} - 2\frac{\partial u_k}{\partial x_k}\Omega + \epsilon_{ijk}\,\frac{\omega_i}{\rho^2}\frac{\partial \rho}{\partial x_j}\frac{\partial p}{\partial x_k} \quad (10b)$$

where $\rho, p, \dot{\omega}, \tau_{ij}$ and $f(D)$ are the density, pressure, chemical source term and viscous stress tensor component and the contributions due to diffusivity gradients, respectively. The terms $-2\rho D\Lambda$ and V are responsible for the generation/destruction of scalar gradients by flame normal straining, and vortex-stretching terms, respectively [9,35,60,67–69]. The terms Λ and V depend on the alignment of ∇c and $\vec{\omega}$ with the most extensive, intermediate and the most compressive principal strain rates (i.e. e_α, e_β and e_γ) in the following manner: $\Lambda = (\partial c/\partial x_i)(\partial u_i/\partial x_j)(\partial c/\partial x_j) = (e_\alpha cos^2\alpha + e_\beta cos^2\beta + e_\gamma cos^2\gamma)\nabla c\cdot\nabla c$ and $V = 2(e_\alpha cos^2\alpha' + e_\beta cos^2\beta' + e_\gamma cos^2\gamma')\Omega$ where α, β, γ (α', β', γ') are the angles between ∇c ($\vec{\omega}$) and the eigendirections associated with e_α, e_β and e_γ respectively. The above expression indicates that a collinear alignment between ∇c ($\vec{\omega}$) and the most extensive principal strain rate e_α (i.e. most positive principal strain rate) leads to $cos^2\alpha = 1$ ($cos^2\alpha' = 1$), which promotes a positive value of Λ (V). By contrast, a collinear alignment between ∇c ($\vec{\omega}$) and the most compressive principal strain rate e_γ (i.e. most negative principal strain rate) leads to $cos^2\gamma = 1$ ($cos^2\gamma' = 1$), which in turn gives rise to negative values of Λ (V).

Fig. 15 shows the contributions of $\langle\Lambda^*\rangle = \langle\Lambda\rangle \times (\delta_Z^3/S_L)$ for individual flow topologies $S1$–$S8$ for cases A, C and E for $Le = 0.8$,1.0 and 1.2 at different time instants. In all cases the total contribution of $\langle\Lambda^*\rangle$ remains positive throughout the flame front when the flame remains away from the wall. However, $\langle\Lambda^*\rangle$ assumes negative values in cases C and E at the late stages of flame quenching. The expression $\Lambda = (e_\alpha cos^2\alpha + e_\beta cos^2\beta + e_\gamma cos^2\gamma)\nabla c\cdot\nabla c$ indicates that a positive (negative) value of this quantity is indicative of preferential alignment of ∇c with the eigenvector associated with the most extensive (compressive) principal strain rate e_α (e_γ). It has been demonstrated elsewhere [60,68,70,71] that ∇c aligns with the most extensive principal strain rate when the strain rate induced by flame normal acceleration overcomes turbulence straining, and conversely preferential alignment of ∇c with e_γ, similar to the case in passive scalar mixing, is obtained when turbulence straining overwhelms the strain rate induced by flame normal acceleration. The strain rate due to flame normal acceleration can be scaled using $\tau S_L/\delta_{th}$, whereas turbulence straining scales as u'/l [60,68,70,71]. For the cases considered here $\tau S_L/\delta_{th}$ remains of the same order but greater than u'/l, and, as a result, straining due to flame normal acceleration dominates over turbulent straining to result in a preferential alignment with the most extensive principal strain rate (and thereby positive values of $\langle\Lambda^*\rangle$) when the flame is away from the wall. The effects of flame normal acceleration weaken after flame quenching and thus ∇c tends to align with the most compressive principal strain rate and in turn gives rise to negative values of $\langle\Lambda^*\rangle$. The effects of turbulent straining is stronger in cases C and E than in case A due to higher u'/S_L, and also due to the fact that the quenching is more advanced stage in case C (case E) than in case A (case C) at a given instant of time (see Table 2). Thus, at final stages of flame quenching $\langle\Lambda^*\rangle$ shows negative values in cases C and E (see $t = 10\delta_Z/S_L$). It can be seen from Fig. 15 that $\langle\Lambda^*\rangle$ contributions conditional on $S2$,$S7$ and $S8$ topologies exhibit positive values, and these topologies offer dominant contributions to $\langle\Lambda^*\rangle$ for all cases when the flame is away from the wall. The $S2$ topology makes the highest contribution to the value of $\langle\Lambda^*\rangle$ for all cases. During flame quenching $\langle\Lambda^*\rangle$ decays significantly when the topologies $S3$ and $S8$ contribute significantly while the contribution of $S2$ topology determines the behaviour of $\langle\Lambda^*\rangle$. The topologies $S7$ and $S8$ are obtained where positive dilatation rate (i.e. thermal expansion) effects are dominant and thus in these locations the strain rate due to thermal expansion dominates over turbulent straining to give rise to a strong alignment between ∇c with e_α which is reflected in the positive contributions of $\langle\Lambda^*\rangle$. The $S1$ topology also makes a dominant positive $\langle\Lambda^*\rangle$ contribution in case E at early times (e.g. $t = 2\delta_Z/S_L$). The topologies $S3$ and $S4$ also exhibit positive values of $\langle\Lambda^*\rangle$ but the magnitudes of these contributions remain smaller than the conditional mean values for $S2$,$S7$ and $S8$ topologies for all cases for $Le = 0.8$ and 1.0. The values of $\langle\Lambda^*\rangle$ conditional on $S3$ and $S4$ topologies exhibit weak negative values for $Le = 1.2$ at early times (e.g. $t = 2\delta_Z/S_L$) in the highest u'/S_L case (i.e. case E), whereas these topologies show positive values for $Le = 0.8$ and 1.0 cases at $t = 2\delta_Z/S_L$ and later times for all cases irrespective of the Lewis number. The effects of thermal expansion are the weakest in the $Le = 1.2$ case among all the Lewis number cases considered here. As a result, turbulent straining overcomes the strain rate induced by flame normal acceleration for the highest u'/S_L case (i.e. case E) with $Le = 1.2$, which leads to preferential alignment of ∇c with e_γ, and thereby negative values of $\langle\Lambda^*\rangle$ are obtained for $S3$ and $S4$ topologies. By contrast, the strain rate induced by flame normal acceleration dominates over turbulent straining for $Le = 0.8$ and 1.0 even in case E and thus positive values of $\langle\Lambda^*\rangle$ are obtained. As time progresses the effects of turbulent straining weaken with the decay of u' and as a result the strain rate due to flame normal acceleration dominates over turbulent strain rate even for case E with $Le = 1.2$ at later times.

The contributions of $\langle V^*\rangle = \langle V\rangle \times (\delta_Z/S_L)^3$ for individual flow topologies $S1$–$S8$ for cases A, C and E are shown in Fig. 16 for $Le = 0.8$,1.0 and 1.2 at different time instants. It can be seen that $\langle V^*\rangle$ remains predominantly positive away from the wall, but this quantity assumes negative values close to the wall. The negative value of $\langle V^*\rangle$ at

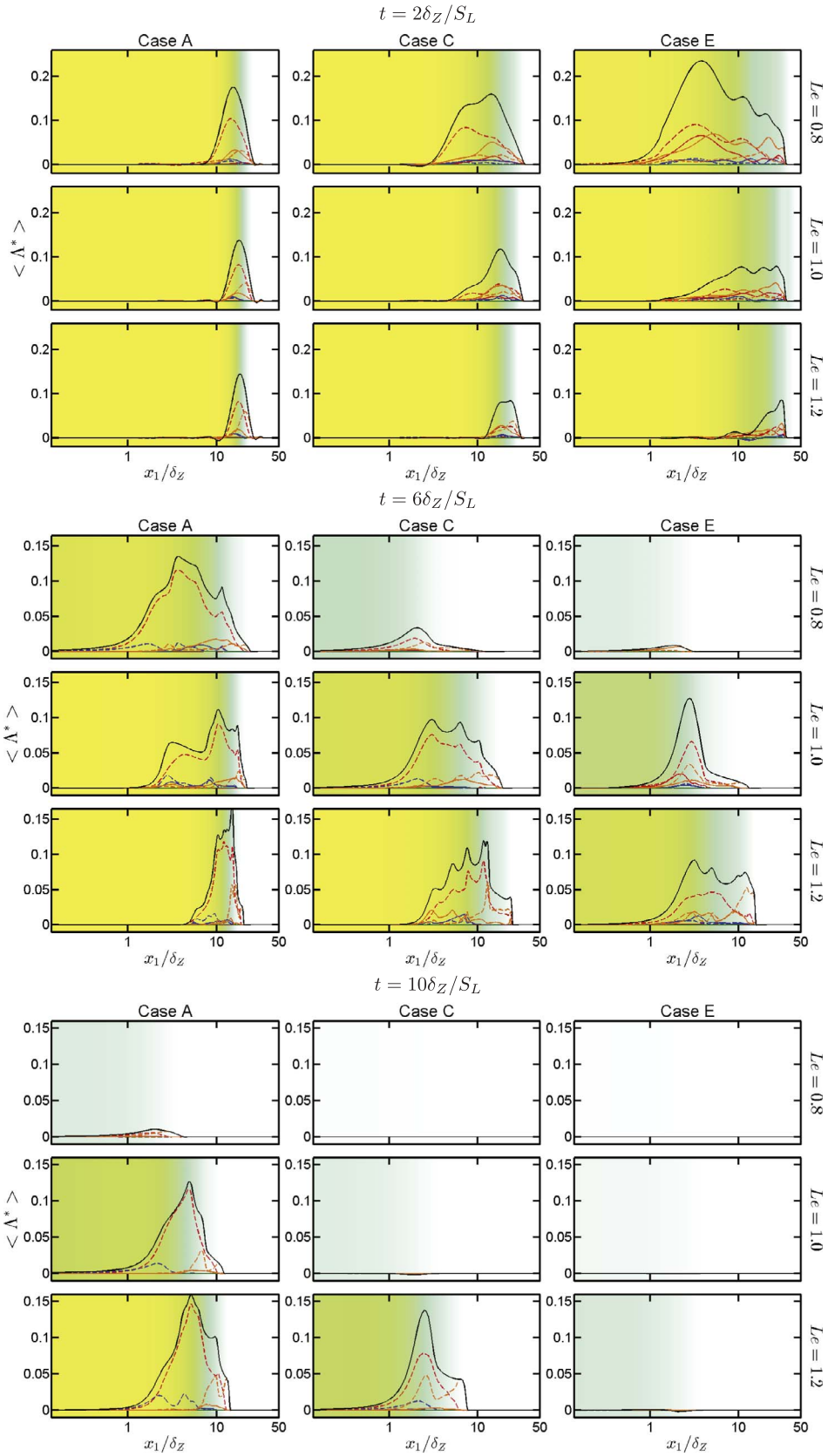

Fig. 15. Variations of $\langle \Lambda^* \rangle = \langle \Lambda \rangle \times \delta_Z^3/S_L$ (——) with x_1/δ_Z for $t = 2\delta_Z/S_L$, $6\delta_Z/S_L$, $10\delta_Z/S_L$ for cases A, C and E with Le = 0.8,1.0 and 1.2 (Focal topologies S1 (——), S4 (——), S5 (——), S7 (——), nodal topologies S2 (— —), S3 (— —), S6 (— —), S8 (— —)).

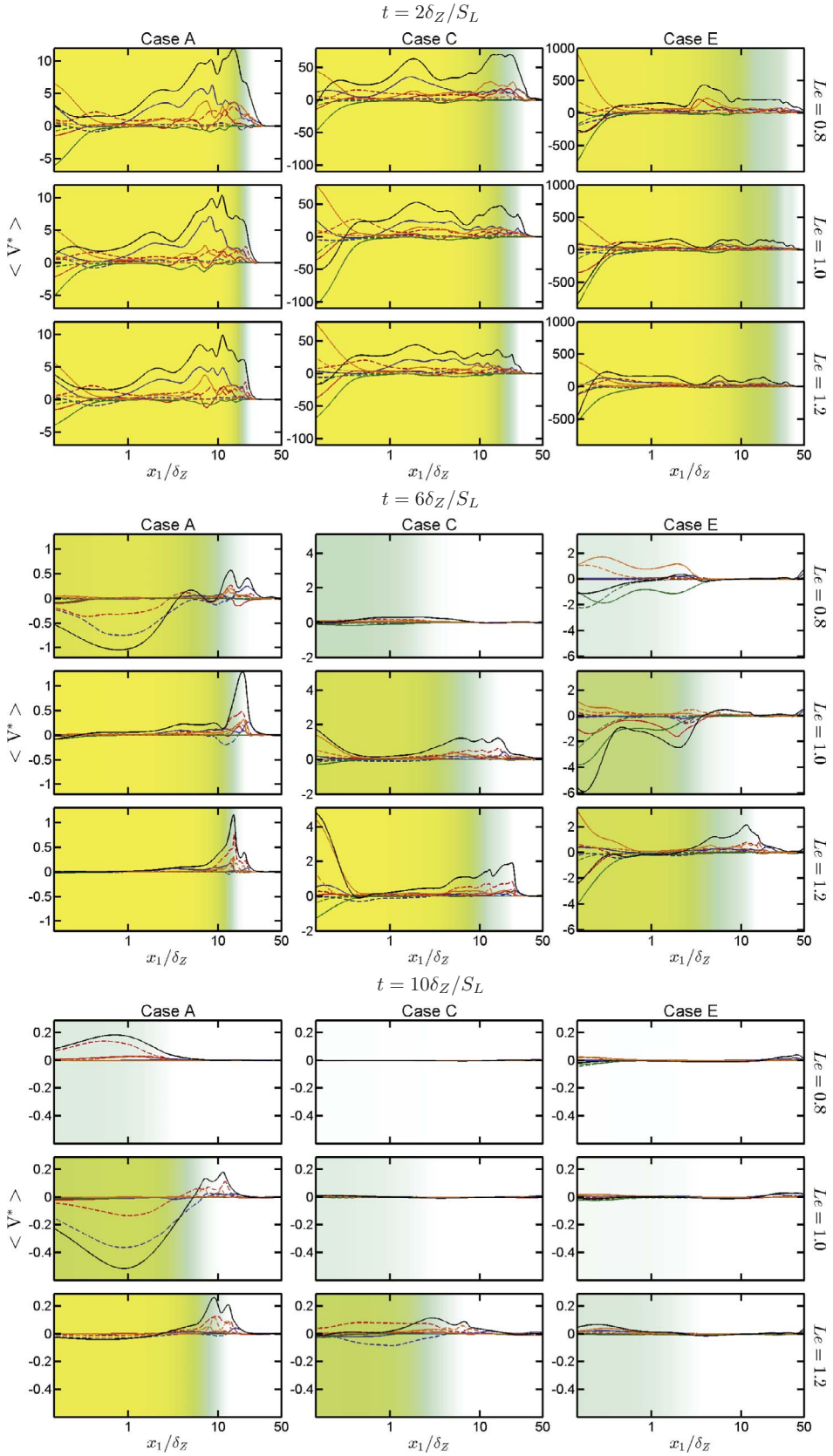

Fig. 16. Variations of $\langle V^* \rangle = \langle V \rangle \times (\delta_Z/S_L)^3$ (——) with x_1/δ_Z for $t = 2\delta_Z/S_L, 6\delta_Z/S_L, 10\delta_Z/S_L$ for cases A, C and E with Le = 0.8,1.0 and 1.2 (Focal topologies S1 (——), S4 (——), S5 (——), S7 (——), nodal topologies S2 (— —), S3 (— —), S6 (— —), S8 (— —)).

the near-wall region becomes increasingly prominent as the time progresses. It has been demonstrated elsewhere [35] that the alignment of vorticity $\vec{\omega}$ with the most compressive principal strain rate e_γ strengthens in the near-wall region, whereas $\vec{\omega}$ preferentially aligns with the intermediate and most extensive principal strain rates (i.e. e_β and e_α) away from the wall. Accordingly, $\langle V^* \rangle$ shows positive values away from the wall and negative values in the vicinity of it. It can be seen from Fig. 16 that the topology $S7$, which is a focal topology associated with stretching (see Fig. 1), shows positive value of $\langle V^* \rangle$ even at the wall for all cases at $t = 2\delta_Z/S_L$ and $6\delta_Z/S_L$, which is indicative of predominant $\vec{\omega}$ alignment with the intermediate and most extensive principal strain rates for this flow topology. The contribution of $\langle V^* \rangle$ arising from $S8$ topology induces positive values of $\langle V^* \rangle$ even at the vicinity of the wall for case E with $Le = 0.8$ at early times (e.g. $t = 2\delta_Z/S_L$). The $S4$ topology, which is also a focal topology associated with stretching becomes the leading order contributor to $\langle V^* \rangle$ away from the wall at early times (e.g. $t = 2\delta_Z/S_L$), but the contribution of $\langle V^* \rangle$ arising from $S4$ decreases in magnitude close to the wall but still remains positive. The negative value of $\langle V^* \rangle$ at the wall arises due to $S1$,$S5$ and $S6$ topologies. The contributions of nodal topologies $S2$ and $S3$ lead to predominantly negative values of $\langle V^* \rangle$ for case A with $Le = 0.8$ ($Le = 1.0$) at $t = 2\delta_Z/S_L$ ($6\delta_Z/S_L$), whereas $\langle V^* \rangle$ conditional on $S2$ exhibits positive values at the final stage of quenching (e.g. $t = 10\delta_Z/S_L$) for case A with $Le = 0.8$ and also for case C with $Le = 1.2$. The observations made from Fig. 16 indicates that the focal topologies associated with stretching tend to promote a positive value of $\langle V^* \rangle$, whereas the negative values of $\langle V^* \rangle$ especially at the wall originate principally due to nodal topologies. A comparison between Figs. 12 and 16 indicates the distributions of focal and nodal topologies determine the nature of $\langle V^* \rangle$ variation in all cases considered here.

The instantaneous wall heat flux can be expressed as $q_w = -\lambda(\partial \widehat{T}/\partial x_1)_{x_1=0}$, where λ is the thermal conductivity. The normalised wall heat flux magnitude is defined here as $\Phi = |q_w|/[\rho_0 S_L C_P(T_{ad}-T_0)]$ [22,30]. Fig. 17a shows the temporal evolutions of maximum, mean and minimum values of Φ for the turbulent cases. It can be seen from Fig. 17 that an increase in u' leads to an increase in maximum wall heat flux magnitude Φ_{max}. A comparison between different Le cases indicates that the maximum heat flux in the turbulent $Le = 0.8$ case is greater than the turbulent $Le \geq 1$ cases. Fig. 4 indicates the existence of thermal inhomogeneity in the burned gas for the non-unity Lewis number flames even before the initiation of flame quenching. Super-adiabatic temperatures ($T > 1$) are observed for non-unity Le cases when the flame is away from the wall. The high (low) values of temperature are associated with the region where the flame curvatures which are convex (concave) towards the reactants for turbulent $Le = 0.8$ cases. An opposite behaviour is observed for the turbulent $Le = 1.2$ cases. Simultaneous strong focusing of reactants and weak defocussing of heat in the turbulent $Le = 0.8$ cases lead to high magnitudes of reaction rate and burned gas temperature in these regions. Just the opposite mechanism gives rise to high temperature values in the regions where flame front is concavely curved towards the reactants for the turbulent $Le = 1.2$ cases. Fig. 2 shows that the flame elements which are convex towards the reactants are likely to reach near the wall at an earlier time. As high temperature zones are associated with the zones which are convex towards the reactants for the $Le = 0.8$ cases, the maximum value of Φ is obtained at an earlier time for smaller values of Le. The flame quenching starts in the turbulent $Le = 0.8$ cases when the super-adiabatic regions reach close to the wall. In these cases, the high rate of chemical reaction enables the convexly curved regions to reach closer to the wall than the corresponding laminar flame-quenching distance, [30] which along with the super-adiabatic temperature gives rise to higher values of maximum wall heat flux magnitude in these cases in comparison to the corresponding turbulent $Le = 1.0$ cases. The super-adiabatic values of temperature in the $Le = 1.2$ cases are associated with the curvatures which are concave towards the reactants and therefore quenching starts before these zones get a chance to interact with the wall. As a result of this, the maximum wall heat flux magnitude for the turbulent $Le = 1.2$ cases remains comparable to the corresponding value for laminar premixed flame-wall interaction [30]. Interested readers are referred to Ref. [30] for further information on wall heat flux statistics for the flames considered here.

The normalised wall heat flux magnitude can be expressed as $\Phi = \Sigma\Phi_{Si}$ where $i = 1{-}8$ with Φ_{Si} being normalised wall heat flux contribution for each individual topology. The fractional contributions of each flow topology towards wall heat flux magnitude (i.e. Φ_{Si}/Φ) are also shown in Fig. 17b for cases A, C and E for different time instants. For cases A–C the wall heat flux magnitude remains small for $t \leq 2\delta_Z/S_L$ as the flame remains sufficiently away from the wall to influence Φ (see Fig. 17). Under this condition, Φ_{Si}/Φ remains comparable for all flow topologies. However, the flame starts to quench by $t = 2\delta_Z/S_L$ in case E with $Le = 0.8$, which is reflected in the temporal increase in wall heat flux magnitude in Fig. 17a. A comparison between Fig. 17a and b reveals that S2 and S3 topologies remain the significant contributors to the overall wall heat flux magnitude during high wall heat flux period during flame quenching (e.g. compare Fig. 17a and b at $t = 6\delta_Z/S_L$ for cases A-E with $Le = 1.0$ and 1.2 and cases A-C with $Le = 0.8$). However, the topologies S6 and S8 become the leading order contributors at the final stage of flame quenching when the wall heat flux magnitude starts to decrease with time (compare Fig. 17a and b at $t = 10\delta_Z/S_L$ for cases A-E with $Le = 0.8$ and 1.0). In general, the nodal topologies have been found to contribute heavily to the wall heat flux magnitude when the flame interacts with the wall during head-on quenching irrespective of the value of global Lewis number.

5. Conclusions

The flow topology distribution and statistical behaviours of the invariants of velocity gradient tensor P,Q and R have been analysed for head-on quenching of statistically planar turbulent premixed flames by isothermal inert walls using three-dimensional DNS data for different values of Lewis numbers at different turbulence intensities u'/S_L and integral length scale to flame thickness ratios l/δ_{th}.The flow topologies have been characterised by the first, second and third invariants (i.e. P,Q and R) of the velocity gradient $\partial u_i/\partial x_j$ tensor. The first invariant is the negative of dilatation rate (i.e. $(\partial u_i/\partial x_i) = -P$) and thus assumes significant negative values within the flame (i.e. $0 < c < 1$), but it assumes vanishingly small values outside the flame in both unburned gases and fully burned products in the $Le = 1.0$ cases when the flame remains away from the wall. The positive dilatation rate effects (i.e. effects of negative P) remain significant not only within the flame, but also in the burned gas due to considerable amount of thermal inhomogeneity resulting from imbalance of species and heat diffusion rates in the case of non-unity Lewis number flames even when they are away from the wall. The strengthening of burning leads to an increase in the magnitude of negative contribution of P within the flame with decreasing Le. The effects of positive dilatation rate weaken close to the wall due to flame quenching. The magnitude of the second invariant Q drops significantly across the flame within the burned gases and it changes from positive (i.e. vorticity dominated region) to negative (i.e. strain rate dominated region) in a short span of space depending on local values of $S_{ij}S_{ij}$ and $W_{ij}W_{ij}$. Furthermore, the extent of this intermittent behaviour increases with increasing turbulence intensity. Moreover, the likelihood of obtaining high magnitudes of the third invariant R increases with increasing (decreasing) u'/S_L (Le) and $|R|$ decreases as quenching progresses with time. A dominant negative correlation between Q and R is obtained when the flame is away from the wall but this negative correlation weakens as time progresses and the flame approaches the wall. The distributions of volume fractions of focal ($S1$,$S4$,$S5$,$S7$) and nodal ($S2$,$S3$,$S6$,$S8$) topologies have been investigated in detail.

This paper provides information on the evolution of dominant flow topologies with the progress of head-on quenching. Furthermore, this analysis also provides information about the evolution of dominant

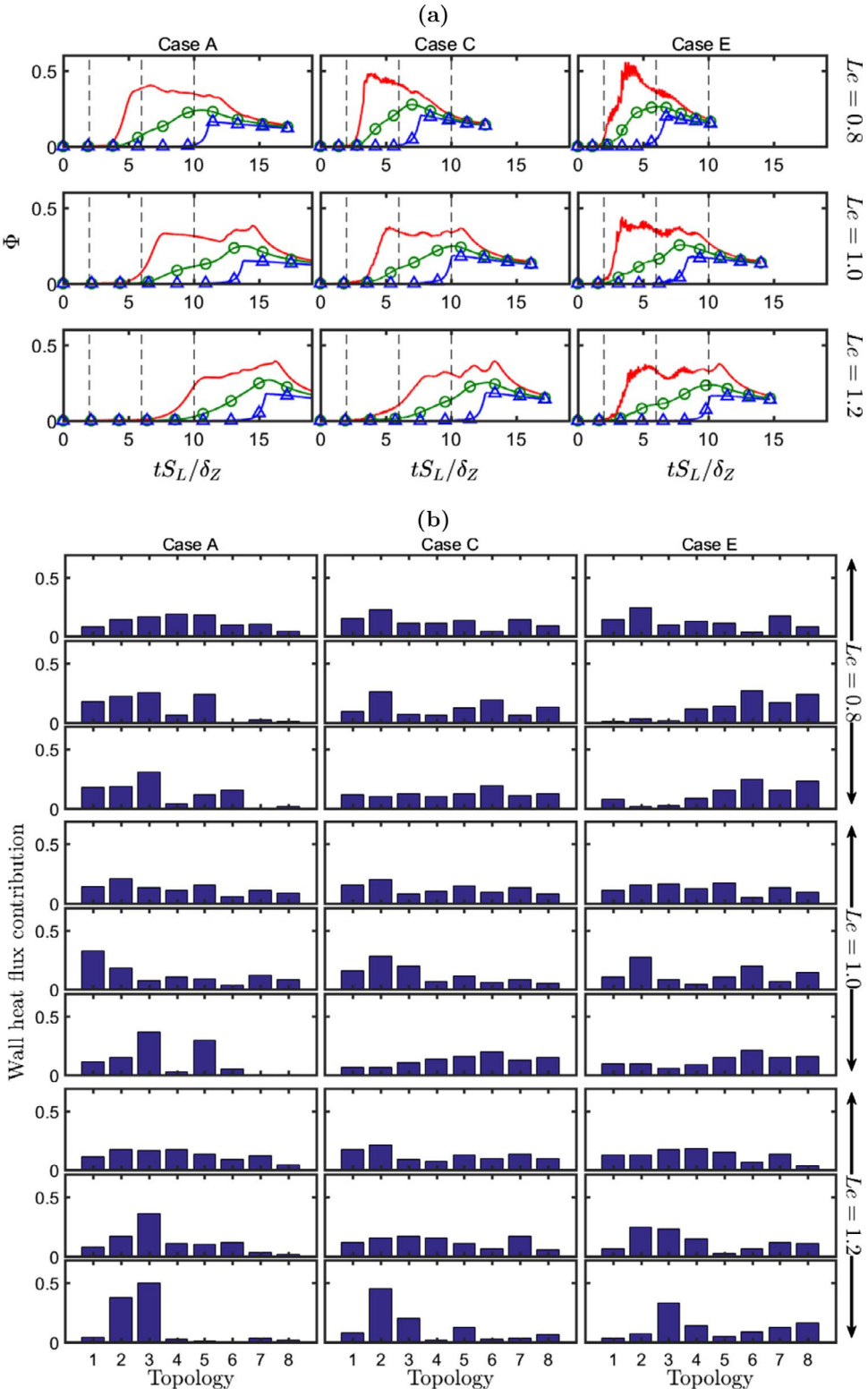

Fig. 17. (a) Temporal evolutions of maximum (—), mean (—○—) and minimum (—△—) values of wall heat flux magnitude Φ for Case A, C and E with Le = 0.8,1.0 and 1.2. Vertical lines indicate time instants for $t = 2\delta_Z/S_L$, $6\delta_Z/S_L$ and $10\delta_Z/S_L$ (left to right) (b) Wall heat flux magnitude contributions from topology $S1$–$S8$ for Le = 0.8,1.0 and 1.2 at different time instant $t = 2\delta_Z/S_L$,$6\delta_Z/S_L$ and $10\delta_Z/S_L$ (top to bottom) with Case A, B and C.

flow topologies contributions to the scalar-turbulence interaction, vortex-stretching terms and wall heat flux during head-on quenching. The volume fraction of focal topologies decreases from the unburned to the burned gas side of the flame front which is consistent with the decay of enstrophy across the flame front in these cases. The decrease (increase) in volume fraction of focal (nodal) topologies across the flame front is less prominent for high values of u'/S_L. It has been found that the flow topologies S7-S8, which are present only for positive values of dilatation rate (i.e. negative values of $-P$), occupy a significant fraction of the flame front when the flame remains away from the wall but the probability of their occurrence drops with the progress of head-on quenching and the topologies S1–S4 (and mainly S2), which are obtained for all possible values of dilatation rate, play dominant roles during flame quenching. The contributions of individual topologies to scalar-turbulence interaction and vortex-stretching terms in the scalar dissipation rate and enstrophy transport equations, respectively have

been analysed. It has been found that the mean scalar-turbulence interaction term $\langle\Lambda\rangle$ remains mostly positive due to predominant alignment of scalar gradient with the most extensive principal strain rate. The $S2$,$S7$ and $S8$ topologies have been found to be leading order contributors to $\langle\Lambda\rangle$, but the contributions of $S7$ and $S8$ topologies weaken close to the wall as these topologies are specific to positive dilatation rate which weakens at the wall due to flame quenching. It has been found that the focal topologies $S4$ and $S7$ associated with stretching promote positive mean values of the vortex-stretching term $\langle V\rangle$, whereas the negative values of $\langle V\rangle$ especially at the wall originate principally due to nodal topologies $S2$ and $S3$. Furthermore $S2$ and $S3$ topologies have been found to the major contributors to the wall heat flux magnitude during flame quenching when high magnitudes of wall heat flux magnitude are obtained. However, $S6$ and $S8$ topologies become the leading contributors to wall heat flux during final stages of flame quenching. The flow topology contributions to wall heat flux remain qualitatively similar for the values *Le* considered here. It can be seen from Fig. 1 that each of these topologies is associated with canonical flow configurations and thus the distributions of the topologies and their contributions to wall heat flux, and the scalar-turbulence interaction and vortex-stretching terms in the scalar dissipation rate and enstrophy transport equations, respectively could be used to design simplified experimental and computational configurations. Moreover, the current analysis indicates that the topologies $S1$–$S4$, which are available for all values of P, play key roles during head-on quenching and out of these topologies $S2$ plays the dominant role. It can be seen from Fig. 1 that the $S2$ topology is representative of the impinging jet configuration. Thus simplified experiments and RANS/LES simulations based on impinging jet configuration will be ideal for obtaining fundamental physical insights into FWI and for model validation in the HOQ configuration. In addition to these simplified analyses, further investigation on flow topology distribution for higher turbulent Reynolds number flows will be necessary for gaining further physical insights.

Acknowledgement

The authors are grateful to N8/ARCHER for computational support.

References

[1] Perry AE, Chong MS. A description of eddying motions and flow patterns using critical-point concepts. Annu Rev Fluid Mech 1987;19(1):125–55.
[2] Chong MS, Perry AE, Cantwell BJ. A general classification of three-dimensional flow fields. Phys Fluids A: Fluid Dyn (1989–1993) 1990;2(5):765–77.
[3] Soria J, Sondergaard R, Cantwell B, Chong M, Perry A. A study of the fine-scale motions of incompressible time-developing mixing layers. Phys Fluids (1994-present) 1994;6(2):871–84.
[4] Blackburn HM, Mansour NN, Cantwell BJ. Topology of fine-scale motions in turbulent channel flow. J Fluid Mech 1996;310:269–92.
[5] Chong M, Soria J, Perry A, Chacin J, Cantwell B, Na Y. Turbulence structures of wall-bounded shear flows found using dns data. J Fluid Mech 1998;357:225–47.
[6] Chacin JM, Cantwell BJ. Dynamics of a low reynolds number turbulent boundary layer. J Fluid Mech 2000;404:87–115.
[7] Ooi A, Martín J, Soria J, Chong M. A study of the evolution and characteristics of the invariants of the velocity-gradient tensor in isotropic turbulence. J Fluid Mech 1999;381:141–74.
[8] Elsinga G, Marusic I. Universal aspects of small-scale motions in turbulence. J Fluid Mech 2010;662:514–39.
[9] Tsinober A. Vortex stretching versus production of strain/dissipation. Turbulence Struct Vortex Dyn 2000:164–91.
[10] Dopazo C, Martín J, Hierro J. Local geometry of isoscalar surfaces. Phys Rev E 2007;76(5):056316.
[11] Chen JH, Cantwell BJ, Mansour NN. The topology and vorticity dynamics of a three-dimensional plane compressible wake. In: Proc. Tenth Australasian Fluid Mechanics Conference; 1989. pp. 5–1.
[12] Sondergaard R, Chen J, Soria J, Cantwell B. Local topology of small scale motions in turbulent shear flows. In: 8th symposium on turbulent shear flows, vol. 1; 1991. pp. 16–1.
[13] Maekawa H, Hiyama T, Matsuo Y. Study of the geometry of flow patterns in compressible isotropic turbulence. JSME Int J Ser B 1999;42(3):336–43.
[14] Suman S, Girimaji SS. Velocity gradient invariants and local flow-field topology in compressible turbulence. J Turbul 2010(11):N2.
[15] Wang L, Lu X-Y. Flow topology in compressible turbulent boundary layer. J Fluid Mech 2012;703:255–78.
[16] Tanahashi M, Fujimura M, Miyauchi T. Coherent fine-scale eddies in turbulent premixed flames. Proc Combust Inst 2000;28(1):529–35.
[17] Grout R, Gruber A, Yoo CS, Chen J. Direct numerical simulation of flame stabilization downstream of a transverse fuel jet in cross-flow. Proc Combust Inst 2011;33(1):1629–37.
[18] Cifuentes L, Dopazo C, Martin J, Jimenez C. Local flow topologies and scalar structures in a turbulent premixed flame. Phys Fluids (1994-present) 2014;26(6):065108.
[19] Cifuentes L. Local flow topologies and scalar structures in turbulent combustion (Ph.D. thesis). University of Zaragoza; 2015.
[20] Wacks D, Chakraborty N. Flow topology and alignments of scalar gradients and vorticity in turbulent spray flames: a direct numerical simulation analysis. Fuel 2016;184(1):922–47.
[21] Wacks DH, Chakraborty N, Klein M, Arias PG, Im HG. Flow topologies in different regimes of premixed turbulent combustion: a direct numerical simulation analysis. Phys Rev Fluids.
[22] Poinsot T, Haworth D, Bruneaux G. Direct simulation and modeling of flame-wall interaction for premixed turbulent combustion. Combust Flame 1993;95(1):118–32.
[23] Bruneaux G, Akselvoll K, Poinsot T, Ferziger J. Flame-wall interaction simulation in a turbulent channel flow. Combust Flame 1996;107(1):27–44.
[24] Bruneaux G, Poinsot T, Ferziger J. Premixed flame–wall interaction in a turbulent channel flow: budget for the flame surface density evolution equation and modelling. J Fluid Mech 1997;349:191–219.
[25] Alshaalan TM, Rutland CJ. Turbulence, scalar transport, and reaction rates in flame-wall interaction. Symposium (International) on Combustion. vol. 27. Elsevier; 1998. p. 793–9.
[26] Alshaalan T, Rutland CJ. Wall heat flux in turbulent premixed reacting flow. Combust Sci Technol 2002;174(1):135–65.
[27] Boust B, Sotton J, Labuda S, Bellenoue M. A thermal formulation for single-wall quenching of transient laminar flames. Combust Flame 2007;149(3):286–94.
[28] Gruber A, Sankaran R, Hawkes E, Chen J. Turbulent flame–wall interaction: a direct numerical simulation study. J Fluid Mech 2010;658:5–32.
[29] Gruber A, Chen JH, Valiev D, Law CK. Direct numerical simulation of premixed flame boundary layer flashback in turbulent channel flow. J Fluid Mech 2012;709:516–42.
[30] Lai J, Chakraborty N. Effects of Lewis number on head-on quenching of turbulent premixed flames: a direct numerical simulation analysis. Flow Turbulence Combust 2016;96(2):279–308.
[31] Lai J, Chakraborty N. Statistical behavior of scalar dissipation rate in head-on quenching of turbulent premixed flames: a direct numerical simulation analysis. Combust Sci Technol 2016;188(2):250–76.
[32] Lai J, Chakraborty N. A priori direct numerical simulation modeling of scalar dissipation rate transport in head-on quenching of turbulent premixed flames. Combust Sci Technol 2016;188(9):1440–71.
[33] Lai J, Chakraborty N. Modeling of progress variable variance transport in head-on quenching of turbulent premixed flames: a direct numerical simulation analysis. Combust Sci Technol 2016;188(11–12):1925–50.
[34] Sellmann J, Lai J, Kempf AM, Chakraborty N. Flame surface density based modelling of head-on quenching of turbulent premixed flames. Proc Combust Inst.
[35] Lai J, Chakraborty N, Lipatnikov A. Statistical behaviour of vorticity and enstrophy transport in head-on quenching of turbulent premixed flames. Eur J Mech-B/Fluids.
[36] Tennekes H, Lumley JL. A first course in turbulence. MIT Press; 1972.
[37] Jenkins KW, Cant RS. Direct numerical simulation of turbulent flame kernels. Recent Advances in DNS and LES. Springer; 1999. p. 191–202.
[38] Chen JH, Choudhary A, De Supinski B, DeVries M, Hawkes ER, Klasky S, Liao W-K, Ma K-L, Mellor-Crummey J, Podhorszki N, et al. Terascale direct numerical simulations of turbulent combustion using s3d. Comput Sci Discovery 2009;2(1):015001.
[39] Poinsot TJ, Lele S. Boundary conditions for direct simulations of compressible viscous flows. J Comput Phys 1992;101(1):104–29.
[40] Wray A. Minimal storage time advancement schemes for spectral methods. NASA Ames Research Center: California, Report No. MS 202.
[41] Rogallo RS. Numerical experiments in homogeneous turbulence, NASA Technical Memorandum 81315. NASA Ames Research Center: California.
[42] Batchelor G, Townsend A. Decay of turbulence in the final period. Proceedings of the Royal Society of London A: Mathematical, Physical and Engineering Sciences. vol. 194. The Royal Society; 1948. p. 527–43.
[43] Peters N. Turbulent combustion. Cambridge University Press; 2000.
[44] Poinsot T, Echekki T, Mungal M. A study of the laminar flame tip and implications for premixed turbulent combustion. Combust Sci Technol 1992;81(1–3):45–73.
[45] Louch D, Bray K. Vorticity in unsteady premixed flames: vortex pair–premixed flame interactions under imposed body forces and various degrees of heat release and laminar flame thickness. Combust Flame 2001;125(4):1279–309.
[46] Aspden A. A numerical study of diffusive effects in turbulent lean premixed hydrogen flames. Proc Combust Inst 2017;36(2):1997–2004.
[47] Sivashinsky G. Diffusional-thermal theory of cellular flames. Combust Sci Technol 1977;15(3–4):137–45.
[48] Clavin P, Williams F. Effects of molecular diffusion and of thermal expansion on the structure and dynamics of premixed flames in turbulent flows of large scale and low intensity. J Fluid Mech 1982;116:251–82.
[49] Pelce P, Clavin P. Influence of hydrodynamics and diffusion upon the stability limits of laminar premixed flames. J Fluid Mech 1982;124:219–37.
[50] Haworth D, Poinsot T. Numerical simulations of Lewis number effects in turbulent

premixed flames. J Fluid Mech 1992;244:405–36.
[51] Rutland C, Trouvé A. Direct simulations of premixed turbulent flames with nonunity Lewis numbers. Combust Flame 1993;94(1):41–57.
[52] Trouvé A, Poinsot T. The evolution equation for the flame surface density in turbulent premixed combustion. J Fluid Mech 1994;278:1–31.
[53] Chakraborty N, Cant R. Influence of Lewis number on curvature effects in turbulent premixed flame propagation in the thin reaction zones regime. Phys Fluids (1994-present) 2005;17(10):105105.
[54] Yuan J, Ju Y, Law CK. Coupled hydrodynamic and diffusional-thermal instabilities in flame propagation at subunity Lewis numbers. Phys Fluids (1994-present) 2005;17(7):074106.
[55] Chakraborty N, Cant R. Influence of Lewis number on strain rate effects in turbulent premixed flame propagation. Int J Heat Mass Transfer 2006;49(13):2158–72.
[56] Chakraborty N, Klein M. Influence of Lewis number on the surface density function transport in the thin reaction zone regime for turbulent premixed flames. Phys Fluids (1994-present) 2008;20(6):065102.
[57] Chakraborty N, Cant R. Effects of Lewis number on scalar transport in turbulent premixed flames. Phys Fluids (1994-present) 2009;21(3):035110.
[58] Chakraborty N, Katragadda M, Cant R. Effects of Lewis number on turbulent kinetic energy transport in premixed flames. Phys Fluids (1994-present) 2011;23(7):075109.
[59] Han I, Huh KY. Roles of displacement speed on evolution of flame surface density for different turbulent intensities and Lewis numbers in turbulent premixed combustion. Combust Flame 2008;152(1):194–205.
[60] Chakraborty N, Klein M, Swaminathan N. Effects of Lewis number on the reactive scalar gradient alignment with local strain rate in turbulent premixed flames. Proc Combust Inst 2009;32(1):1409–17.
[61] Chakraborty N, Swaminathan N. Effects of Lewis number on scalar dissipation transport and its modeling in turbulent premixed combustion. Combust Sci Technol 2010;182(9):1201–40.
[62] Chakraborty N, Swaminathan N. Effects of Lewis number on scalar variance transport in premixed flames. Flow Turbulence Combust 2011;87(2–3):261–92.
[63] Mizomoto M, Asaka Y, Ikai S, Law C. Effects of preferential diffusion on the burning intensity of curved flames. Symposium (International) on Combustion. vol. 20. Elsevier; 1985. p. 1933–9.
[64] Law C, Kwon O. Effects of hydrocarbon substitution on atmospheric hydrogen–air flame propagation. Int J Hydrogen Energy 2004;29(8):867–79.
[65] Dinkelacker F, Manickam B, Muppala S. Modelling and simulation of lean premixed turbulent methane/hydrogen/air flames with an effective lewis number approach. Combust Flame 2011;158(9):1742–9.
[66] Chakraborty N, Lipatnikov A. Effects of Lewis number on the statistics of conditional fluid velocity in turbulent premixed combustion in the context of reynolds averaged navier stokes simulations. Phys Fluids 2013;25(4):045101.
[67] Chakraborty N, Konstantinou I, Lipatnikov A. Effects of Lewis number on vorticity and enstrophy transport in turbulent premixed flames. Phys Fluids (1994-present) 2016;28(1):015109.
[68] Chakraborty N, Champion M, Mura A, Swaminathan N. Scalar dissipation rate approach to reaction rate closure. In: Swaminathan N, Bray KNC, editors. Turbulent premixed flames. Cambridge, UK: Cambridge University Press; 2011.
[69] Chakraborty N. Statistics of vorticity alignment with local strain rates in turbulent premixed flames. Eur J Mech-B/Fluids 2014;46:201–20.
[70] Chakraborty N, Swaminathan N. Influence of the damköhler number on turbulence-scalar interaction in premixed flames. I. Physical insight. Phys Fluids (1994-present) 2007;19(4):045103.
[71] Kim SH, Pitsch H. Scalar gradient and small-scale structure in turbulent premixed combustion. Phys Fluids (1994-present) 2007;19(11):115104.